Simulation of Electron Drift Properties and Track Reconstruction for the Deep Underground Neutrino Experiment

by

Aaron Mutchler

A thesis submitted to the Faculty of the

University of Colorado in partial fulfillment

of the requirements for the award of

departmental honors in the

Department of Physics

March 23, 2021

This thesis entitled:
Simulation of Electron Drift Properties and Track Reconstruction for the Deep
Underground Neutrino Experiment
written by Aaron Mutchler
has been approved for the Department of Physics

_____
Professor Alysia Marino

_____
Professor John Cumalat

_____
Professor Jeanne Clelland

Date _____

The final copy of this thesis has been examined by the signatories, and we find that both
the content and the form meet acceptable presentation standards of scholarly work in the
above mentioned discipline.

Mutchler, Aaron (B.A.,Physics)

Simulation of Electron Drift Properties and Track Reconstruction for the Deep Underground
    Neutrino Experiment

Thesis directed by Professor Alysia Marino

The Deep Underground Neutrino Experiment (DUNE) is a new cutting-edge experiment that will be fundamental in the study of neutrino oscillations and physics beyond the standard model. DUNE will be the flagship neutrino experiment, with the longest neutrino beamline of 1300 kilometers, using state-of-the-art near and far detectors to measure neutrino flavor at the start and end of the beam. In the near detector hall, DUNE will implement a High Pressure Gaseous Argon Time Projection Chamber (HPgTPC). A crucial step in studying oscillations is understanding the flux of neutrinos and their interaction cross-sections in the near detector. Neutrinos will interact with the argon and produce charged particles, which liberate electrons that drift across the HPgTPC. To extract the necessary information about neutrino interactions, details of the drift electrons must be known, such as the drift velocity, diffusion, and attachment. For this thesis, I will simulate electron drift properties in DUNE's HPgTPC. Using the new PyBoltz simulation code, I determine the allowed region of operation for the HPgTPC. With this, I will further study how changes to the electron drift properties, namely the diffusion, will impact the reconstruction efficiency of muon tracks through GArSoft simulation.

Acknowledgements

First and foremost I would like to express how truly grateful and appreciative I am of Professor Alysia Marino for giving me this opportunity and mentoring me for two years. Not everyone is able to get involved with research, and I am glad I had the chance to do so through Professor Marino. I learned a lot from her and I am grateful for her patience as I have and continue to learn. I also want to thank Dr. Andrew Cudd for all the help he provided me when my simulations broke and for helping me understand new topics. Next, I would like to acknowledge my other thesis committee members, Professor Jeanne Clelland and Professor John Cumalat. Thank you for helping honors work come together. Thank you Professor Clelland for being an awesome teacher for me. Thank you to my friends and family who helped me get to this point and were sounding boards for me to flush out my thoughts. Thank you mom and dad for always pushing me to be my best and give my best, if you had not I would not be here. Lastly, a thank you to Squishy sticking with me through all the late nights of homework and writing.

Contents

Chapter

Tables

Table

Figures

Figure

Chapter 1

Introduction

Everything in the known, observable universe is composed of matter. In contrast, there is also antimatter which annihilates ordinary matter when the two interact. Moreover, the current assumption is that matter and antimatter comprised the universe in equal parts at its start [1]. If this is true, why then today is matter dominant over antimatter? This is known as matter/antimatter asymmetry. The building blocks of matter and antimatter, fermions, and force-carrying particles, bosons, together make up the Standard Model. Although this model has been successful, it is incomplete and physicists are still on the search for 'physics beyond the Standard Model.'

One peculiar detail about the Standard Model is that it describes neutrinos as massless particles. What makes this peculiar is that in an attempt to measure the flux of neutrinos from the Sun, the experimental result was about a third of the expected value [2]. This became known as the 'solar neutrino problem.' Once the scientific community recognized the neutrino and determined that they were produced during fusion in stars, scientists sought to measure those neutrinos produced from the Sun traveling toward Earth. What the researchers found, however, was about one third of the expected value. The exciting solution to this problem was the discovery that three different types (flavors) of neutrinos exist and they can *change* their flavor, or oscillate, as a function of energy and distance traveled. This is a major discovery because neutrino oscillations can only occur with a nonzero and distinct masses relative to one another. Furthermore, in 1967, violation of charge-parity

(CP) emerged as a possible explanation for matter/antimatter asymmetry [1]. This means that a process such as a neutrino of flavor X oscillating to flavor Y may have a different rate of occurrence than its anti-particle counterpart: anti-neutrino flavor X oscillating to anti-neutrino flavor Y [1]. Studying the oscillation rate of neutrinos and anti-neutrinos will establish CP violation in the lepton sector, furthering our understanding of the matter/anti-matter asymmetry.

In another pressing issue, physicists have sought to unify the fundamental forces of nature since the nineteenth century. Huge steps have been made with the unification of electricity and magnetism and a theory for combing the electromagnetic force with strong and weak forces known as Grand Unified Theory (GUT). Some experiments suggest these forces were united at the start of the universe. Current GUT's, working to unify electromagnetic, strong, and weak forces require a process known as proton decay, which has yet to be observed [1], [3].

Neutrinos are the most ample matter particle, and as mentioned earlier, one way to produce neutrinos is through fusion in stars. The Earth is under constant bombardment from these stellar neutrinos. When a stellar core collapses and goes supernova, neutrinos are produced in abundance.[1] This is known to be true, even though the dynamics of supernovae are not well understood [3]. Using neutrinos as an early signal we can look to study supernovae.

The matter/antimatter asymmetry, proton decay, and core collapse supernovae will be investigated by the Deep Underground Neutrino Experiment (DUNE) through the precision study of neutrino oscillations. DUNE, with the Long Baseline Neutrino Facility (LBNF), will be able to take high-statistic studies of oscillations through the most intense neutrino beam. Key to these studies are state-of-the-art far and near detectors (FD and ND, respectively) to measure the neutrino flavor at the start of the beam and again at the end. The FD and ND will implement gaseous and liquid argon time projection chamber technology

---

[1] $\sim 10^{57}$ neutrinos

to reconstruct tracks with high resolution. The FD will deploy four massive, liquid argon time projection chambers[2] [4], [5]. The ND will consist of three detectors: ND-LAr, ND-GAr, and SAND. Starting from the upstream position, the ND-LAr will operate similarly to the FD (see Figure 3.4). Next is the ND-GAr which consists of a high pressure gaseous argon time-projection chamber (HPgTPC), surrounded by an electromagnetic calorimeter (ECAL), all of which will be encased by superconducting magnet coils. To best perform track reconstruction in the HPgTPC, drift properties of electrons in the ND-GAr must be well understood. Specifically, drift properties at high pressure under various conditions are not well known.

This thesis will present research on how variations in the HPgTPC affect electron drift properties and how this, in turn, affects simulated track reconstruction efficiency. Altering conditions of the HPgTPC including variables such as temperature, pressure, applied electric and magnetic fields, and gas composition all directly impact how electrons drift throughout the detector. Chapter 2 will describe the fundamental theory behind neutrinos and their oscillations. Chapter 3 will focus on DUNE, its goals, and the ND. Next, Chapter 4 will give a detailed description of time-projection chambers. Chapter 5 will describe the simulation tools used. Chapter 6 and 7 will present findings on drift properties of the HPgTPC and effects on simulated track reconstruction efficiency respectively.

---

[2]   40 kt fiducial volume in total

<center>

Chapter 2

Neutrinos: Fundamentals

</center>

2.1 What are Neutrinos?
A Historical Introduction

Before the 1950's neutrinos were particles unobserved by humans. It was not until Wolfgang Pauli postulated the neutrino[1] as a solution to beta decay dilemma. The process for simplistic beta decay is as follows: $n \rightarrow p + e^-$, a neutron decays into a proton and an electron. However, this process overturns the fundamental idea of conservation of angular momentum because the left-hand side of the reaction has a total intrinsic angular momentum of 1/2, whereas the right-hand side has a intrinsic angular momentum of 1. To make matters worse, experimental data showed this process lead to a loss of energy: violating conservation of energy. Some suggested conservation was statistical or that we should reject these ideas; instead Pauli posited the idea of a third unidentified particle to save conservation laws [6]. Shortly after, Enrico Fermi developed a more complete theory for beta decay and coined the term 'neutrino' as we understand it today.

With Fermi's developed theory of the neutrino, beta decay can now be properly described as:

$$n \rightarrow p + e^- + \overline{\nu}_e,$$
$$p \rightarrow n + e^+ + \nu_e, \tag{2.1}$$

---

[1] He named it 'neutron', however J. Chadwick got to the name first[6].

where $\overline{\nu}_e$ is the antiparticle to the electron neutrino, ν_e [2], [6]. Fermi's work solved the beta decay dilemma and saved conservation laws. From Pauli, to Fermi, to today, physicists have, and continue to, study and develop more complete theories of neutrinos: to their incorporation in the Standard Model.

2.2 The Standard Model

Aside from neutrinos, the universe is composed of many other fundamental particles all of which are organized into a table known as the Standard Model as shown in Figure 2.1. All the fundamental particles can be grouped into spin-1 force mediators, known as bosons, or spin-1/2 matter particles, known as fermions.

Figure 2.1: The Standard Model: a description of the fundamental interactions on quarks (blue) and leptons (green) through force carrying bosons (red) and the Higgs boson (gray). This model can be extended to incorporate the anti-particles as well[7].

2.2.1   Bosons

The force carrying particles (shown in red in Figure 2.1) are the gluon (g), photon (γ), $W^{\pm}$ and Z bosons, and they mediate the strong force, electromagnetic force, and weak force respectively.[2] There is also gravity, where scientists have hypothesized the force is mediated by a particle called the graviton. However, this has yet to be incorporated into the Standard Model. The relative strength of these forces in shown in Table 2.1.

Relative Strength of Fundamental Forces		
Force	**Mediator**	**Relative Strength**
Strong	gluon g	10^{38}
Electromagnetic	photon γ	10^{36}
Weak	$W^{\pm}$ and Z bosons	10^{25}
Gravity	graviton (hypothesized)	1

Table 2.1: This table summarizes the fundamental forces and their strengths relative to the gravitational force [1].

Given the strength of the fundamental forces if a particle can go through a process in multiple ways, the strongest available force will dominate.

An important property of these force mediators is charge. Particles can have either electric charge, color charge, both, or neither. The gluon, photon, and Z boson have no electric charge whereas the $W^{\pm}$ bosons do with electric charge $+1$ and -1 respectively. The gluon is the only boson with color charge and all others are 'colorless'. If a particle has color charge it can take on the color red, green, or blue.[3] These force carries couple to the matter particles.

---

[2]   The Higgs boson is a spin 0 boson and does not directly mediate the fundamental forces.

[3]   In order for the gluon to couple to all quarks and conserve color charge in interactions, there are eight different color super-positions of quarks.

2.2.2 Fermions

Fermions can be further subdivided into either quarks or leptons. Quarks come in six types: up, down, charm, strange, top, and bottom. Each quark has electric charge. the up, charm, and top have electric charge $+\frac{2}{3}$e, whereas the down, strange, and bottom have electric charge $-\frac{1}{3}$e. The quark's electric charge allows them to couple to photons and interact electromagnetically. Quarks also have color charge, allowing them to couple to gluons, as such they can take a color charge of red, green, or blue. They form bound states[4] into mesons (quark-anti-quark pair) or baryons (three quarks or three anti-quarks) [8].[5] Probably the most familiar hadrons are nuclei: protons and neutrons. These are baryons as they are made from a bound state of three quarks (uud and ddu respectively). Quarks can interact via all fundamental forces (strong, weak, and electromagnetic).

As mentioned in Chapter 1, leptons come in three different 'flavors': electron, muon, and tau. For each flavor particle there is a corresponding neutrino. Similar to quarks, the electron, muon, and tau leptons all have electric charge -1e, and so they can interact electromagnetically. The neutrinos are neutrally neutral and so cannot interact electromagnetically. Unlike quarks, leptons do not have color charge so they will not interact strongly. All leptons can interact weakly [1], [8]. Bosons and fermions are all brought together through particle interactions which we can picture with Feynman diagrams.

2.2.3 Interactions

Richard Feynman created a way to visualize and understand how the particles of the Standard Model interact and are mediated with the so called Feynman diagrams. These diagrams are built up of fundamental interaction vertices and are read along the time axis: from left to right. The other axis (up-down on the page) is 'space-like', we can think of the particles moving through space in this dimension. At each vertex all conservation laws

---

[4]   Bound states of quarks are referred to as hadrons [8].

[5]   Tetraquark and pentaquark groups have been proposed but have yet to be observed experimentally.
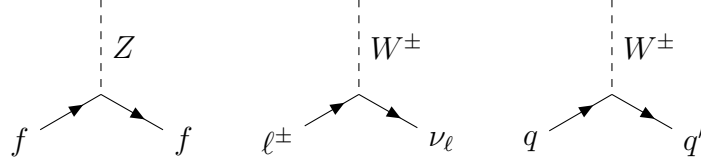
Figure 2.2: The three primary interaction vertices for the weak force: Z vertex (left), W vertex for leptons (middle), and W vertex for quarks (right).

apply. Feynman diagrams can be drawn vertically (as shown below), this is referred to as a 'T-channel', or they can be drawn horizontally, which is known as an 'S-channel'. As neutrinos are of main concern here, only the fundamental weak vertex will be explained. This is followed by some example Feynman diagrams involving neutrinos that will be discussed in later chapters.

Shown below are the fundamental Feynman vertex diagrams for the weak interaction, to which all fermions can couple. The three possible vertices for the weak interaction are shown in Figure 2.2. The Z interaction vertex (left) is off minimal interest because neutrinos cannot be detected in this way, even though they can interact through exchange of a Z boson. Shown in the middle is the $W^\pm$ vertex for leptons. Given the charge of the W boson the lepton, ℓ, must change to a neutrino but of the same lepton flavor, ν_ℓ following charge and lepton number conservation. The rightmost diagram of Figure 2.2 is the W vertex for quarks. Again, due to the electric charge of the W, charge conservation requires that the incoming and exiting quark are different by one unit of charge. In this way quarks can change from one type to another through weak interactions. Figure 2.3 depicts Feynman diagrams for several possible neutrino interactions. On the left is the process of beta decay as described above. In the middle is the leptonic decay of a π^+ meson to a muon neutrino, ν_μ, and an anti-muon, μ^+. Lastly, on the right is the interaction of an anti-muon neutrino with a proton. Pion decay and anti-neutrino interactions will be explained in Chapters 3 and 4 respectively.
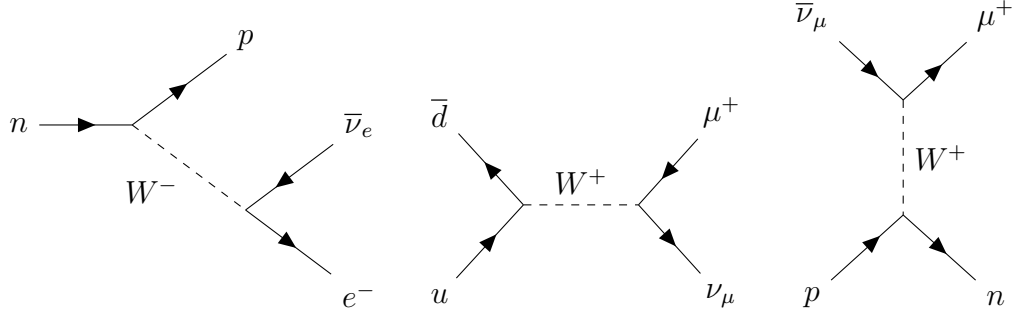
Figure 2.3: A few possible neutrino interactions. Beta decay (left), Leptonic decay of a pion, π^+, (middle). The interaction of an anti-muon neutrino, $\overline{\nu}_\mu$, with a proton, p, (right).

2.3   CP Violation

So far the Standard Model has performed well in describing natural phenomena. It also raises questions about potential conserved quantities. An intuitive guess for a first symmetry would be spatial inversion, (mirror symmetry): physical process are invariant if it is spatially flipped that is $\vec{r} \to -\vec{r}$.[6] This is known as 'parity symmetry'. Another is charge-conjugation in which the particle is flipped to its anti-particle counterpart.[7]

Parity will flip the particle's momentum $(\vec{p} \to -\vec{p})$ but not the spin. One could ask then, how to the spin and momentum vectors line up? The projection of a particle's spin along its momentum is known as helicity. If the particle is massless (or sufficiently small in the case of neutrinos) helicity and handedness are the same. So, if the spin and momentum point in opposite directions then the particle is said to have 'left-helicity' or to be 'left-handed'. On the other hand, a particle whose spin and momentum align and point in the same direction is said to have 'right-helicity' or to be 'right-handed'. Key to the present discussion is the fact that $W^\pm$ and Z bosons couple to left-handed neutrinos and right-handed anti-neutrinos [1]. For parity to be conserved, the mirror image of the reaction should occur as often as the original reaction. That is, particles who are left-handed in the original reaction should

---

[6] $\hat{P}|r\rangle = -|r\rangle$

[7] $\hat{C}|particle\rangle = |\overline{particle}\rangle$

be right-handed in the mirror reaction. It has been shown that parity is conserved in strong and electromagnetic interactions but theorists T. D. Lee, C. N. Yang, and C. S. Wu and her team found that parity was maximally violated in weak interactions [9], [10].

Wu *et al.* test for parity symmetry involved beta decay which brings in the issue that weak interactions only couple to left-handed particles so perhaps applying a charge conjugation to the process will make it invariant preserving the symmetry. This is known as 'Charge-parity' (CP). As mentioned above charge-conjugation takes a particle to its anti-particle counterpart and like parity is conserved in strong and electromagnetic interactions. As it turns out investigation of reaction rates between neutral Kaons ($K^0 \leftrightarrow \overline{K^0}$) shows that CP is slightly violated in weak interactions [1], [5].

Hence, CP violation partially accounts for the matter/antimatter asymmetry. CP violation in the lepton sector of the Standard Model can be observed through neutrinos oscillations.

2.4   Oscillations

With the creation of the Standard Model, neutrinos were thought to be massless. However, as mentioned in Chapter 1, this cannot be true given the detection of neutrino oscillations. For neutrinos to oscillate it must be that the flavor eigenstates (ν_e, ν_μ, ν_τ) are linear combinations of three other states and hence not eigenstates of the particles' free space Hamiltonian. These other states, call them ν_1, ν_2, and ν_3, are then the mass eigenstates with masses m_1, m_2, and m_3 respectively. Since the flavor eigenstates can be written as linear combinations of the mass eigenstates, so too should the mass eigenstates be represented as a linear combination of the flavor eigenstates [1]. This mixing then between the mass and flavor eigenstates is what causes neutrinos to oscillate. Before discussing three-flavor oscillations, a simplified model of two-flavor oscillations is presented.

2.4.1   Two-Flavor Oscillations

To understand the basic process, consider just an electron and muon neutrino, ν_e and ν_μ. As described above the mass eigenstates can be written as:

$$|\nu_1\rangle = \cos(\theta)|\nu_\mu\rangle - \sin(\theta)|\nu_e\rangle, \tag{2.2a}$$

$$|\nu_2\rangle = \sin(\theta)|\nu_\mu\rangle + \cos(\theta)|\nu_e\rangle, \tag{2.2b}$$

$$\implies \begin{pmatrix} \nu_1 \\ \nu_2 \end{pmatrix} = \begin{pmatrix} \cos(\theta) & -\sin(\theta) \\ \sin(\theta) & \cos(\theta) \end{pmatrix} \begin{pmatrix} \nu_e \\ \nu_\mu \end{pmatrix}, \tag{2.2c}$$

where θ is a mixing angle describing how much each flavor eigenstate composes a mass eigenstate and the 2×2 matrix in 2.3c is the mixing matrix.[8] Note that there is a bijection between the mass and flavor states so Equation 2.2 can be rewritten using the inverse of the mixing matrix. The inverse of this matrix is equivalent to its transpose conjugate so it is unitary. Rewriting Equation 2.2 as

$$\begin{pmatrix} \nu_e \\ \nu_\mu \end{pmatrix} = \begin{pmatrix} \cos(\theta) & \sin(\theta) \\ -\sin(\theta) & \cos(\theta) \end{pmatrix} \begin{pmatrix} \nu_1 \\ \nu_2 \end{pmatrix} \tag{2.3}$$

brings the problem into the eigenbasis, which is necessary to determine the time dependence of the states.

Since ν_1 and ν_2 are the mass eigenstates, with eigenvalues E_1 and E_2 respectively, the time dependence is determined by simply solving the Schrödinger equation. This yields

$$|\nu_e(t)\rangle = \cos(\theta)e^{-i\frac{E_1 t}{\hbar}}|\nu_1\rangle + \sin(\theta)e^{-i\frac{E_2 t}{\hbar}}|\nu_2\rangle, \text{ and } |\nu_\mu\rangle = -\sin(\theta)e^{-i\frac{E_1 t}{\hbar}}|\nu_1\rangle + \cos(\theta)e^{-i\frac{E_2 t}{\hbar}}|\nu_2\rangle.$$

In order to understand the oscillation between the two flavor states it is necessary to fix the neutrino to one flavor state, determine the time dependence then find the projection of the time-dependent state onto the second flavor state. Suppose then the particle starts out as an electron neutrino and let $|\psi(t)\rangle$ describe the neutrino throughout this process. That is to

---

[8]   By using cos and sin the eigenstates are appropriately normalized.

say $|\psi(0)\rangle = |\nu_e\rangle = \cos(\theta)|\nu_1\rangle + \sin(\theta)|\nu_2\rangle$. It follows then

$$|\psi(t)\rangle = \cos(\theta)e^{-i\frac{E_1 t}{\hbar}}|\nu_1\rangle + \sin(\theta)e^{-i\frac{E_2 t}{\hbar}}|\nu_2\rangle, \tag{2.4}$$

and rotating back into the flavor basis gives

$$|\psi(t)\rangle = \left(\cos^2(\theta)e^{-i\frac{E_1 t}{\hbar}} + \sin^2(\theta)e^{-i\frac{E_2 t}{\hbar}}\right)|\nu_e\rangle + \left(\sin(\theta)\cos(\theta)e^{-i\frac{E_2 t}{\hbar}} - \cos(\theta)\sin(\theta)e^{-i\frac{E_1 t}{\hbar}}\right)|\nu_\mu\rangle. \tag{2.5}$$

So the probability of starting as an electron neutrino and flipping to a muon neutrino is given by

$$P_{\nu_e \to \nu_\mu} = |\langle \nu_\mu|\psi(t)\rangle|^2 = (\sin(\theta)\cos(\theta))^2\left(e^{-i\frac{E_2 t}{\hbar}} - e^{-i\frac{E_1 t}{\hbar}}\right)\left(e^{i\frac{E_2 t}{\hbar}} - e^{i\frac{E_1 t}{\hbar}}\right)$$
$$= \left[\sin(2\theta)\sin(\omega_{21}t)\right]^2, \tag{2.6}$$

where $\omega_{21} = \frac{E_2 - E_1}{\hbar}$ is the oscillation frequency dependent on the energy difference. Before going further, introducing natural units, $c = 1 = \hbar$, simplifies some of the mathematics. In order to but understand the oscillation frequency, the energy eigenvalues can be solved for: $E_i = \sqrt{(p)^2 + (m_i)^2}$. Using the fact that neutrinos are highly relativistic, that is $m \ll p$ so p can be treated as constant, and Taylor-expanding reveals that $E_i \approx p + \frac{(m_i)^2}{2p}$. Again using the relativistic limit for momentum $p = E$, so the energy difference becomes: $\frac{1}{2E}(m_2^2 - m_1^2)$. Also note that $t \approx L$, where L is the distance the neutrino has travel, traveling at approximately the speed of light (which is 1 here). In conclusion, the oscillation probability can be rewritten as

$$P_{\nu_e \to \nu_\mu} = \left[\sin(2\theta)\sin\left(\frac{(m_2^2 - m_1^2)L}{4E}\right)\right]^2, \tag{2.7}$$

and it is clear to see here that the neutrino oscillation is a function of how much energy it has, E, and the distance it has traveled, L. This means that, given a neutrino with some nonzero energy, at a distance of $L = \frac{2\pi E}{(m_2^2 - m_1^2)}$ the initial electron neutrino is most likely to change to a muon neutrino [1], [2], [11].

2.4.2 Full Three-Flavor Oscillations

In working to understand neutrino oscillations with three flavors, most of the hard work has been done in the previous section. Fundamentally three flavor oscillation is the same as two flavor oscillations only the mathematics becomes more complicated as the mixing matrix between mass and flavor states has to be expanded for the extra flavor. Physicists Ziro Maki, Masami Nakagawa, and Shoichi Sakata developed the three-flavor mixing matrix which is called the Pontecorvo–Maki–Nakagawa–Sakata (PMNS), and similar to two-flavor oscillation it is unitary [5]. As above the flavor eigenstates are mixture of the mass eigenstates described with the PMNS mixing matrix as $\vec{\nu}_\alpha = \mathbf{U}\vec{\nu}_i$ ($\alpha = e, \mu, \tau$ the flavor states, $\mathbf{U}$ the PMNS matrix, and $i = 1, 2, 3$ the mass states), or

$$\begin{pmatrix} \nu_e \\ \nu_\mu \\ \nu_\tau \end{pmatrix} = \begin{pmatrix} U_{e1} & U_{e2} & U_{e3} \\ U_{\mu 1} & U_{\mu 2} & U_{\mu 3} \\ U_{\tau 1} & U_{\tau 2} & U_{\tau 3} \end{pmatrix} \begin{pmatrix} \nu_1 \\ \nu_2 \\ \nu_3 \end{pmatrix}, \tag{2.8}$$

where $\mathbf{U}$ is given by

$$\mathbf{U} = \begin{pmatrix} c_{12}s_{13} & c_{13}s_{12} & s_{13}e^{-i\delta_{CP}} \\ -s_{12}c_{23} - c_{12}s_{23}s_{13}e^{i\delta_{CP}} & c_{12}c_{23} - s_{12}s_{23}s_{13}e^{i\delta_{CP}} & s_{23}c_{13} \\ s_{12}s_{23} - c_{12}c_{23}s_{13}e^{i\delta_{CP}} & -c_{12}s_{23} - s_{12}c_{23}s_{13}e^{i\delta_{CP}} & c_{23}c_{13} \end{pmatrix}. \tag{2.9}$$

Here $c_{ij} = \cos(\theta_{ij})$, $s_{ij} = \sin(\theta_{ij})$, and θ_{ij} is the mixing angle between the mass eigenstates i and j, and (most importantly) the CP-violating phase δ_{CP}. This phase would be 0 or π if oscillations did not violate CP-symmetry [3], [5], [12]. The PMNS matrix can be decomposed into three matrices where each one is a projection along each mass eigenstate:

$$\begin{pmatrix} U_{e1} & U_{e2} & U_{e3} \\ U_{\mu 1} & U_{\mu 2} & U_{\mu 3} \\ U_{\tau 1} & U_{\tau 2} & U_{\tau 3} \end{pmatrix} = \begin{pmatrix} 1 & 0 & 0 \\ 0 & c_{23} & s_{23} \\ 0 & -s_{23} & c_{23} \end{pmatrix} \begin{pmatrix} c_{13} & 0 & s_{13}e^{-i\delta_{CP}} \\ 0 & 1 & 0 \\ -s_{13}e^{i\delta_{CP}} & 0 & c_{13} \end{pmatrix} \begin{pmatrix} c_{12} & s_{12} & 0 \\ -s_{12} & c_{12} & 0 \\ 0 & 0 & 1 \end{pmatrix}. \tag{2.10}$$

Starting with a neutrino of one flavor, α, $|\psi(0)\rangle = |\nu_\alpha\rangle = U_{\alpha 1}|\nu_1\rangle + U_{\alpha 2}|\nu_2\rangle + U_{\alpha 3}|\nu_3\rangle$. Its time dependence is given as (again in natural units)

$$|\psi(t)\rangle = U_{\alpha 1}e^{-iE_1 t}|\nu_1\rangle + U_{\alpha 2}e^{-iE_2 t}|\nu_2\rangle + U_{\alpha 3}e^{-iE_3 t}|\nu_3\rangle. \tag{2.11}$$

Then oscillating to another flavor, β, is given by (following the same process as before)

$$\begin{aligned} P_{\nu_\alpha \to \nu_\beta} &= |\langle \nu_\beta | \psi(t)\rangle|^2 \\ &= \left| \sum_{i=1}^{3} U_{\beta i} \overline{U}_{\alpha i} e^{-iE_i t} \right|^2 \\ &= \delta_{\alpha\beta} - 4\sum_{i<j} \mathrm{Re}\left(U_{\alpha i}\overline{U}_{\beta i}\overline{U}_{\alpha j}U_{\beta j} \sin^2\left(\frac{\omega_{ij}L}{2E}\right)\right) \\ &\quad + 2\sum_{i<j} \mathrm{Im}\left(U_{\alpha i}\overline{U}_{\beta i}\overline{U}_{\alpha j}U_{\beta j} \sin\left(\frac{\omega_{ij}L}{2E}\right)\right). \end{aligned} \tag{2.12}$$

Where (as before) solving for the energy eigenvalues and taking the difference, $E_i - E_j$, yields

$$\begin{aligned} (E_i - E_j)t &\approx \frac{(m_i^2 - m_j^2)}{2p}t \\ &= \frac{L}{2E}\Delta m_{ij}^2, \end{aligned} \tag{2.13}$$

again using $t \approx L$, $p \approx E$, and Δm_{ij}^2 is just the difference of the squared masses, therefore $\omega_{ij} = \frac{\Delta m_{ij}^2}{2}$ [3], [5], [11]–[13]. It is evident then that the oscillation probability is dependent on:

(1) the mixing angles, $\theta_{ij}, i < j$,

(2) the CP-violating phase, δ_{CP},

(3) the difference of masses squared, $\Delta m_{ij} = m_i^2 - m_j^2$,

(4) the distance the neutrino has traveled, L, and

(5) the energy of the initial neutrino, E.

The discussion cannot end here as neutrino oscillation experiments seek to quantify charge-parity violation in the lepton sector so it is imperative to ask about oscillations from an

$\overline{\nu}_\alpha \to \overline{\nu}_\beta$ oscillations as well. A quick peak reveals that

$$
\begin{aligned}
P_{\overline{\nu}_\alpha \to \overline{\nu}_\beta} &= |\langle \overline{\nu_\beta} | \overline{\psi}(t) \rangle|^2 \\
&= \delta_{\alpha\beta} - 4 \sum_{i<j} \mathrm{Re} \left(\overline{U}_{\alpha i} U_{\beta i} U_{\alpha j} \overline{U}_{\beta j} \sin^2 \left(\frac{\omega_{ij} L}{2E} \right) \right) \\
&\quad + 2 \sum_{i<j} \mathrm{Im} \left(\overline{U}_{\alpha i} U_{\beta i} U_{\alpha j} \overline{U}_{\beta j} \sin \left(\frac{\omega_{ij} L}{2E} \right) \right).
\end{aligned}
\tag{2.14}
$$

Equations 2.12 and 2.14 are identical unless **U** contains a complex CP-violating phase δ_{CP} different from zero and π. The CP-asymmetry is estimated by a parameter $\mathcal{A}_{CP}^{\alpha \to \beta}$ given as [14]

$$
\mathcal{A}_{CP}^{\alpha \to \beta} = \frac{P_{\nu_\alpha \to \nu_\beta} - P_{\overline{\nu}_\alpha \to \overline{\nu}_\beta}}{P_{\nu_\alpha \to \nu_\beta} + P_{\overline{\nu}_\alpha \to \overline{\nu}_\beta}},
\tag{2.15}
$$

where in the case of muon to electron neutrino oscillations can be approximated by

$$
\mathcal{A}_{CP}^{\alpha \to \beta} \approx \sin \delta_{CP} \frac{\cos \theta_{23} \sin 2\theta_{12}}{\sin \theta_{23} \sin \theta_{13}} \left(\frac{\Delta m_{21}^2 L}{4E} \right).
\tag{2.16}
$$

Ergo, the existence of a nonzero (and non-π) phase factor, δ_{CP}, in the PMNS matrix reveals that $P_{\nu_\alpha \to \nu_\beta} \neq P_{\overline{\nu}_\alpha \to \overline{\nu}_\beta}$ [5], [14], [15]. If $\delta_{CP} = \pm \frac{\pi}{2}$ then CP is maximally violated.

The Deep Underground Neutrino Experiment will create a muon neutrino beam and look for oscillations to electron neutrinos. Figure 2.4 shows the oscillation probabilities for an initial muon neutrino for both large (left) and small (right) $\frac{L}{E}$.
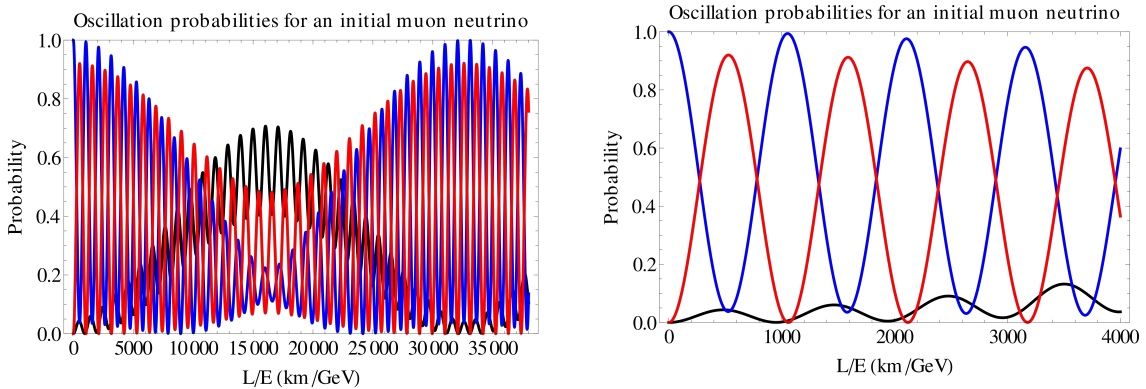

Figure 2.4: Neutrino oscillation probabilities. The blue, red, and black curves are muon, electron, and tau flavors respectively. Plots retrieved from [12].

2.4.3   Neutrino Mass Ordering

The frequency of oscillations in both two and three flavors is dependent on $\Delta m_{ij}^2 = m_i^2 - m_j^2$. This result implies that that the three masses must be distinct otherwise no oscillation can occur. Therefore if one is has zero mass, the other two cannot and therefore all neutrinos cannot be massless as originally thought. It is tempting to try and solve each m_i, however, only the square mass difference can be determined. This introduces the neutrino mass ordering as shown in Figure 2.5. The masses must have some relation $m_i < m_j < m_k$ which can be determined through Δm_{ij}^2 measurements. Given the definition of the difference of the masses squared, there are only two independent parameters say $\Delta m_{sol}^2 = \Delta m_{21}^2$ and $\Delta m_{atm}^2 = \Delta m_{32}^2$. Solar neutrino oscillations are governed by Δm_{sol}^2, where solar neutrino experiments have determined that $\Delta m_{sol}^2 > 0$ so $m_1 < m_2$. Likewise, atmospheric neutrinos, those produced from cosmic ray showers, have oscillations dependent on Δm_{atm}^2. Atmospheric neutrino experiments have determined $|\Delta m_{atm}^2| > |\Delta m_{sol}^2|$. Understanding the relation between Δm_{atm}^2 and Δm_{sol}^2 does not force a mass ordering, however. Current experiments seek to determine the sign of Δm_{atm}^2 (and therefore the sign of Δm_{31}^2), where a positive gives the normal ordering or a negative sign gives the inverted ordering [16], [17].
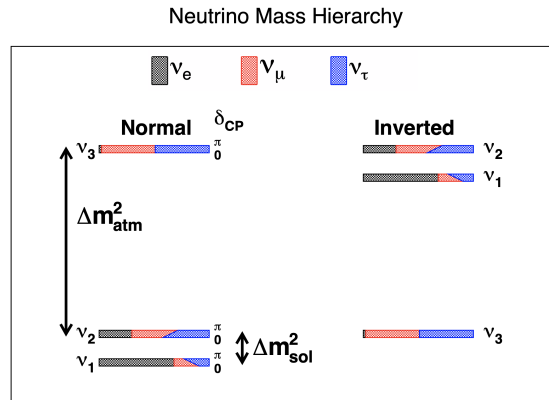

Figure 2.5: Possible mass ordering for neutrinos. Retrieved from [18].

Chapter 3

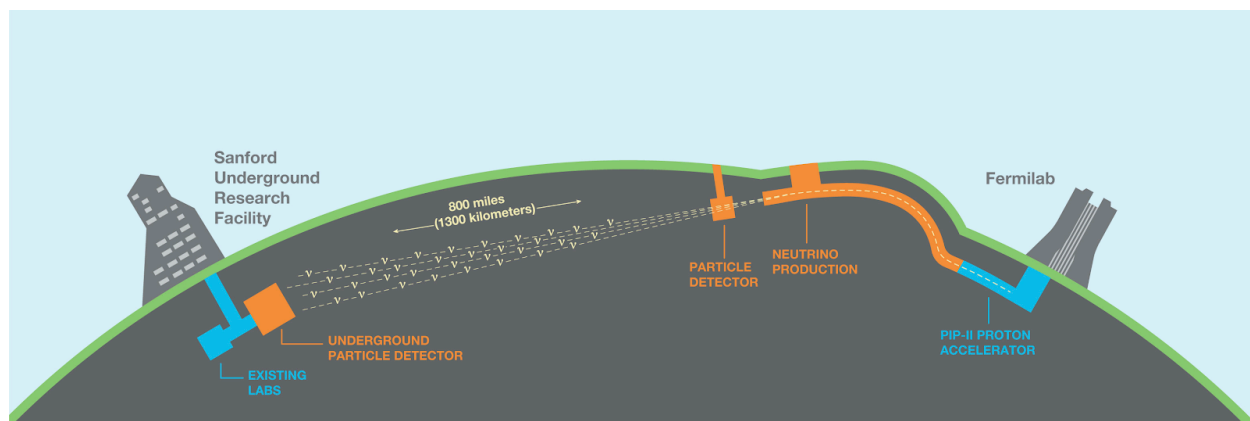## The Deep Underground Neutrino Experiment

Figure 3.1: An illustration of DUNE's beamline from Fermilab to SURF. Graphic retrieved from [19].

The Deep Underground Neutrino Experiment (DUNE) will be the flagship neutrino experiment. It is a massive undertaking and requires the work of over 1000 collaborations from over 30 countries. DUNE will implement the world's most intense particle beam while also maintaining the longest neutrino baseline yet. The neutrino beam will be produced at the Long-Baseline Neutrino Facility (LBNF) at Fermilab in Illinois and travel 1300 km[1] through the Earth, to the Sanford Underground Research Facility (SURF) in South Dakota as shown in Figure 3.1 [19]. The experiment is scheduled to begin taking data in the mid to late 2020's. This experiment will study many things but has three primary goals.

---

[1]   800 miles

3.1   The Goals of DUNE

As mentioned in Chapter 1, DUNE has three primary objectives [4]:

(1) precision measurement of $\nu_\mu \to \nu_e$, and $\overline{\nu}_\mu \to \overline{\nu}_e$ neutrino oscillations,

(2) search for proton decay and,

(3) detection and measurement the ν_e flux from core-collapse supernova.

3.1.1   Precision Measurement of Neutrino Oscillations

As previously mentioned, neutrino oscillations are the key to showing CP violation in the lepton sector of the Standard Model. If the CP violation phase, δ_{CP} is equal to 0 or π then there is no violation of CP in the lepton sector, otherwise this nonzero/non-π result might explain the cause for the matter-antimatter asymmetry.

Studying neutrino oscillations will allow the neutrino mass ordering to be appropriately determined: either the standard or inverted ordering. This means determining the sign of $\Delta m_{31}^2 = m_3^2 - m_1^2$.

Lastly, DUNE's precision measurement of neutrino oscillations will also test for three-flavor oscillations by measuring muon neutrino disappearance and electron neutrino appearance. This will help in determining the mixing angle[2] θ_{23} [3].

3.1.2   Search for Proton Decay

Preluded in Chapter 1, GUT's have been developed to unify three of the four fundamental forces but not without consequence. Current GUT's predict that protons should decay, however, this has not yet been observed. DUNE will search for several different processes for proton decay including $p \to K^+ \overline{\nu}$. Discovery of this or another proton decay mode would be groundbreaking and help push for the unification of the fundamental forces [3].

---

[2]   As discussed in Chapter 2.

3.1.3   Supernova Physics

Supernovae are rare phenomenon and as such little is known about them. Should any occur during the lifetime of DUNE, it will measure the electron neutrino flux from a core-collapse supernova. DUNE can measure the time, flavor, and energy of the supernova neutrino burst and these measurements will help develop our understanding [3].
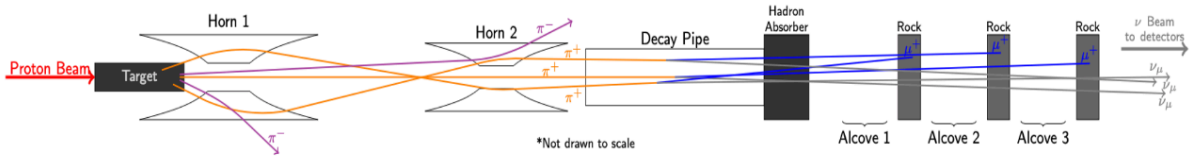
3.2   How the Beamline is Made

Figure 3.2: This is a schematic of the NuMI beam and how DUNE will make its neutrino beam.

In order to make precision measurement of neutrino oscillations, DUNE will need a high-intensity collimated beam of neutrinos. To accomplish this, protons will be be accelerated near the speed of light, with energies in the range of 60 - 120 GeV, then smashed into a graphite target. The process of creating DUNE's beamline is depicted in Figure 3.2. Due to the relativistic speeds of the incoming protons the byproducts of the collision will already be focused in the general direction desired for the experiment. The highly relativistic collisions at the graphite target will produce mesons. These mesons are mostly pions, which will undergo leptonic decay to produce neutrinos [16].

Once the pions are produced the magnetic horns focus the beam and filter out either the π^+ or π^- to create an anti-neutrino beam or neutrino beam respectively. This happens

via the pion decay as described by

$$\pi^+ \rightarrow \mu^+ + \nu_\mu, \tag{3.1a}$$

$$\pi^- \rightarrow \mu^- + \overline{\nu}_\mu, \tag{3.1b}$$

and is also depicted in Figure 3.3. After the desired pions are selected they traverse the decay pipe where the decay products: muons and neutrinos are produced. Thus the neutrino beam is created. The hadron absorber and three alcoves serve to filter out muons and other decay products, purifying the beam.
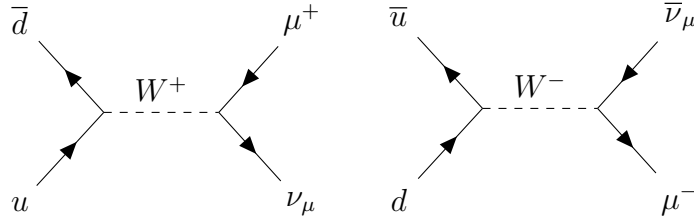

Figure 3.3: Feynman diagrams showing the decay of a π^+ (left) to an anti-muon and muon neutrino, and the decay of a π^- (right) to a muon and anti-muon neutrino through the weak interaction.

As shown in Figure 3.2, muons will make it through the hadron absorber into the alcoves. DUNE will take advantage of these charged particles, using them to monitor the beam so the neutrinos are on target for the far and near detectors.

3.3 The Far Detector

As mentioned in Chapter 1, DUNE will deploy four liquid argon time projection chambers approximately 1.5km underground whose mass will be approximately 17.5kt. Each of the four detectors will be approximately 15.1 (width)$\times$14 (height) $\times$62 (length) cubic meters [4]. Placing the detectors so far away from the surface of the Earth will shield the detectors

from cosmic rays and other radiation that would otherwise interfere with the detector of neutrinos. These detectors will be responsible for the detection of electron and muon neutrinos.

The FD will be located at SURF in South Dakota which is about 930 miles from Fermilab and the start of the beam. As the beam travels this is about 800 miles. The time projection chamber technology will be explained in detail in Chapter 4.
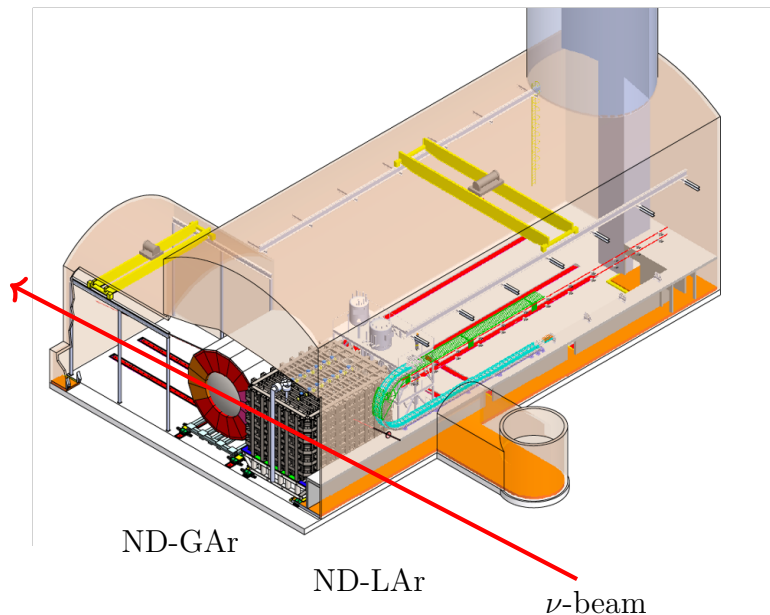
3.4   The Near Detector

Figure 3.4: DUNE's near detector hall and the neutrino path (red). Both the ND-GAr and ND-LAr will be able to slide in and out of the beam path.[3]

Before the neutrinos flavor measurements can be made at the FD, the flavor of the incident beam must be known. The near detector (ND) will be located at Fermilab just downstream of the alcoves shown in Figure 3.2. The ND's primary purpose is in constraining the systematic uncertainties in DUNE's oscillation studies [3], [4]. Given the immense

---

[3]   Again SAND not pictured here.

neutrino flux at the ND, DUNE will also use it to [3]:

- advance the precision measurement of neutrino interactions including cross sections, exclusive processes, electroweak and isospin physics, and nuclei structure, and

- search for new physics including sterile neutrinos and large Δm^2 oscillations among others.[4]

There are three detectors that comprise the near detector hall, as shown in Figure 3.4. From upstream to downstream they are ND-LAr, ND-GAr, and SAND. The ND-LAr is a liquid argon time projection chamber similar to the FD but on a much smaller scale.[5] It is the main target for the incoming neutrinos and serves as the experimental control for the FD. The SAND detector is an on axis beam monitor that will use scintillating plastic [4].

3.4.1   ND-GAr

Second in the beamline at the ND hall, and the location for the studies of this thesis, is the ND-GAr. This detector will be responsible for obtaining high resolution momentum measurement of particles that exit the ND-LAr, and resolving neutrino interactions on argon gas with low momentum thresholds [4], [20].

Neutrinos that interact in the ND-LAr will produce muons and these, along with other interaction byproducts, will exit the detector. These particles[6] will then enter the ND-GAr where where they can be measured. Unlike the ND-LAr, the ND-GAr has a magnetic field which allows for energy and momentum measurements of particles traversing it. One of the important aspects of the ND-GAr is to track and provide precision measurement of muon momenta who are produced from neutrino interactions in the ND-LAr. With the magnetic field, the curvature of the muons tracks can be measure and the sign of the muons can be determined. Where a muon that curves up as it passes through the ND-GAr has positive

---

4   Sterile neutrinos are hypothesized to be neutrinos interacting only via gravity.
5   only 7 (width)×3 (height)×5 (depth) cubic meters [20]
6   as well as all of the neutrinos that did not interact in the ND-LAr

charge (μ^+), likewise a muon that curves down has negative charge (μ^-). Along with muon momenta measurements, the ND-GAr will provide more information on neutrino interactions on argon atoms. The interaction events in the ND-GAr can be detected with a lower threshold than the ND-LAr as the gaseous argon has a lower density and allows for longer particle ranges.
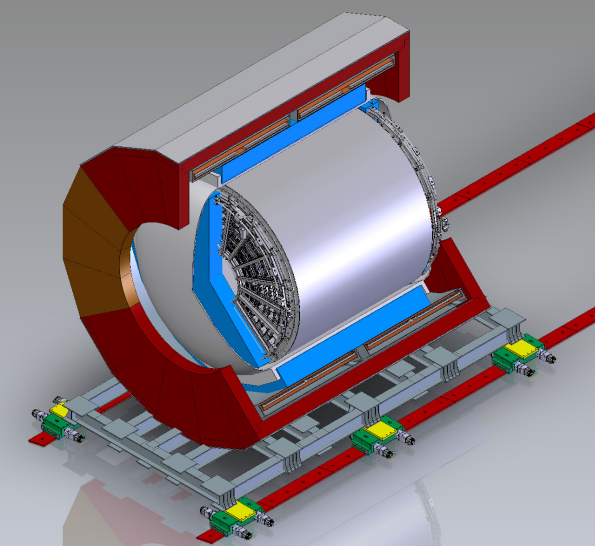
A close up of the ND-GAr is shown in Figure 3.5. The detector is composed of three separate parts, from outside- in they are:

(1) a superconducting magnet coil,

(2) an electromagnetic calorimeter (ECAL), and

(3) the High Pressure gaseous argon Time Projection Chamber (HPgTPC).

Figure 3.5: The ND-GAr detector with the HPgTPC (grey, inside), ECAL (blue), and superconducting magnet (red, outside).

The superconducting magnet coil will supply a magnetic field of 0.5 T to the HPgTPC, allowing the detector to make momentum measurement of particles. Enclosed by the superconducting magnet is the ECAL. It is responsible for collecting the energy of e^+/e^- and $\gamma's$ that exit the HPgTPC. These particles will enter the detector and shower depositing all their energy. The ECAL is composed of 2×2 cm^2 tiles and will also allow for reconstruction of neutrons created from neutrino interactions in the HPgTPC [4]. Lastly, enclosed by both the superconducting magnet and ECAL is the HPgTPC. As discussed in chapter 4, where the workings of the HPgTPC will be explained, this detector will be based on the design of the TPC from the ALICE experiment at CERN and is shown in Figure 4.4.

Chapter 4

Particle Detection

If neutrinos are so evasive, only interacting weakly, how is it possible to detect them? Force interactions to occur by manufacturing a neutrino beam with a large flux and put high density objects in the neutrinos' path. This has been done with chlorine, as in the Ray Davis *et al.* experiment,[1] water, as in the T2K experiment, and DUNE will use liquid and gaseous argon [1].

Fundamental particles can be detected several ways, but this discussion will focus on ionization detectors. The main idea behind ionization detectors is that a charged particle knocks loose charge from the medium of the detector (ionization), and then the liberated charge are collected. Some types of ionization detectors are: proportional counters, ionization chambers, Geiger-Müller counter, multi-wire proportional chamber, and time projection chambers, to name a few [21]. Of these, the time projection chamber is most prevalent to this discussion and so will be explored in further detail.

---

[1]   This was done in the first detection of neutrinos from the Sun in 1968. The detector was located in a mine in South Dakota and looked for argon atoms in the chlorine [1].

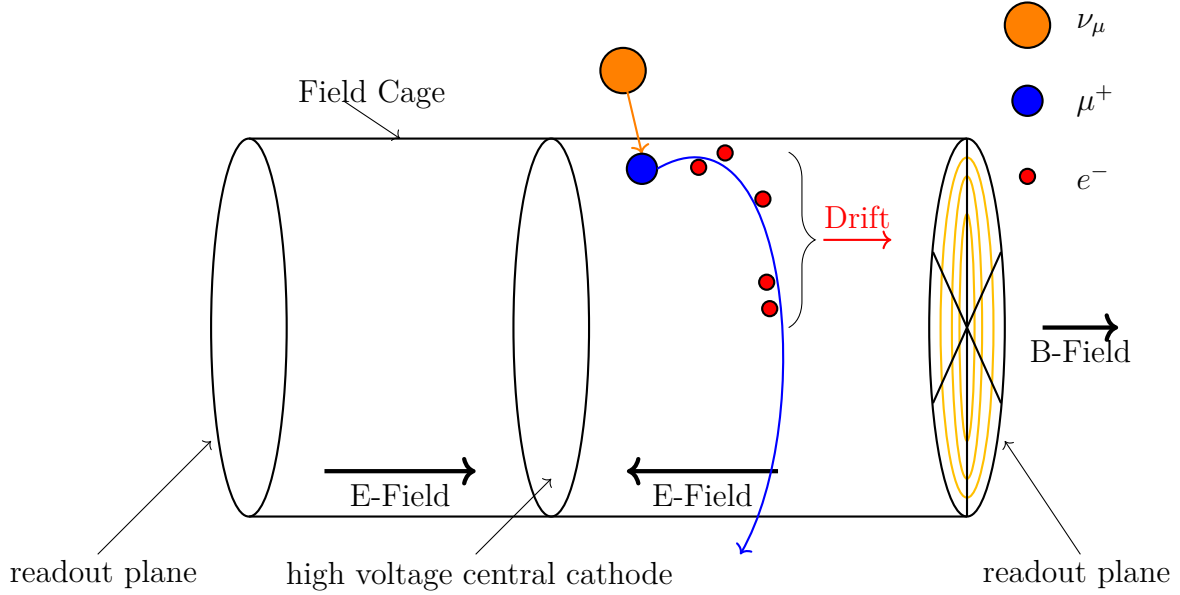## 4.1   Time Projection Chamber Technology at DUNE

Figure 4.1: A toy model of DUNE's HPgTPC.

An example layout of a time projection chamber (TPC) is shown in Figure 4.1. Starting with a cylindrical symmetric object, the end-caps of the detector are composed of wires and grids forming readout planes. In the center of the detector is a high voltage central cathode plane. The cathode plane creates an electric field in the detector in which the field lines point from the readout planes to the central cathode. Along the outside of the detector in discrete steps from the readout plane to the central cathode are resistors to make the electric field as uniform as possible, commonly referred to as the field cage. Outside the detector, a superconducting magnet will supply a magnetic field aligned with the electric field.[2] The detector is then filled with a gaseous or liquid mixture as previously mentioned.

When a neutrino enters the detector, it will most likely punch through as if nothing was there and continue on its way. This is expected, and desired, because neutrinos need to make it to the FD for a complete study of neutrino oscillations. However, there is a nonzero

---

[2]   Not all TPCs have a magnetic field applied to them, see section 3.4.1 for more details.
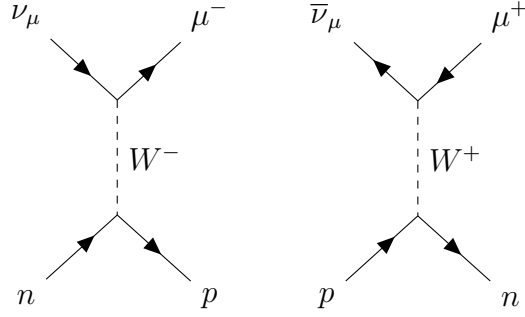
Figure 4.2: Neutrino (left) and anti-neutrino (right) interactions inside a TPC. The weak interaction causes the neutron to change to a proton or visa versa.[3]

probability the neutrino will weakly interact with the argon gas inside the detector through the exchange of a $W^{\pm}$ boson, shown in Figure 4.2. In these special cases, the neutrino will produce a charged lepton. The charged lepton produced depends on the flavor of the incident neutrino. In DUNE, for example (and shown in Figure 4.1), a muon neutrino produces a muon. This newly created particle will then traverse the TPC (taking a curved path under the influence of the magnetic field) and exit. Because the produced lepton was charged, it will deposit energy as it travels in the form of ionized electrons. These liberated electrons will occasionally have sufficient energy to ionize more of the TPCs medium, producing secondary electrons. This will not happen every time however. Then, in the presence of the electric field, the primary and secondary electrons will drift up the electric field lines. As they do so, they will spiral around the magnetic field lines in a helix until finally reaching the readout plane. Once here, the electrons will be collected on wires, and image charges are projected on pads behind them, giving a readout voltage.

In TPCs it is assumed that until the readout plane, electrons will drift at constant velocity. A constant drift velocity, with a known drift time means the drift length can be extrapolated. The drift length combined with the two dimensional signal from the readout plane gives particle information in three dimensions, hence, time projection chamber. Once

---

[3] That is to say an up quark changes to a down in a anti-neutrino proton interaction or a down quark changes to an up in a neutrino neutron interaction.

the signal, and all deposited energy, has been collected, tracks can be reconstructed. Using the fact that the amount of charge collected is proportional to the amount of energy lost, particles can be identified with the Bethe-Bloch formula. Along with this, the magnetic field causes charged particles to curve and this can be used to determine the sign of the charge given the Lorentz force law $F = q\left(\vec{E} + \vec{v} \times \vec{B}\right)$.

Once particles are freed many mechanisms affect the particles drift properties such as drift velocity, diffusion, and attachment. The drift properties and what influences them are discussed below.

4.2   Electron Diffusion

After a charged particle has liberated electrons, there will be an electron cloud in the TPC. This electron cloud will immediately start to diffuse. In the absence of an electric field, the freed electrons will diffuse symmetrically in the form of a Gaussian [22]. The diffusion of of N electrons after time t in a segment dx is given by

$$\frac{dN}{dx} = \frac{N_0}{\sqrt{4\pi Dt}} e^{\frac{-x^2}{4Dt}}, \tag{4.1}$$

where D is the linear diffusion coefficient given by

$$D = \frac{v\lambda}{3} = \frac{2}{3P\sigma_0}\sqrt{\frac{(k_bT)^3}{\pi m}}. \tag{4.2}$$

Here λ is the mean free path, $\frac{k_bT}{\sqrt{2}\sigma_0 P}$, k_b is Boltzmann's constant, T is the temperature of the gas, and σ_0 is the collision cross-sectional area, dependent on gas molecules, and P is the pressure. From this we can write down the speed of the diffusion and a ratio of the diffusion to the mobility:

$$\begin{aligned} v &= \sqrt{\frac{8k_bT}{\pi m}}, \\ \frac{D}{\mu} &= \frac{k_bT}{e}. \end{aligned} \tag{4.3}$$

The last equality comes from defining the mobility of electrons to be $\mu = \frac{v}{E}$. The root mean square of the spread of diffusion in one dimension and three dimensions is given by

$$\sigma_x = \sqrt{2Dt}, \text{ and } \sigma_V = \sqrt{6Dt}. \tag{4.4}$$

This will change if an electric field is present, however. The electric field will alter diffusion in the direction of the E-field. We can break up the diffusion into transverse and longitudinal components, D_L and D_T. The longitudinal component, D_L, is in the direction of the E-field. For the E-field of DUNE ND-GAr $D_L = D_x$, $D_T = \sqrt{(D_z)^2 + (D_y)^2}$. Then the spread of the electrons becomes

$$\sigma_L = \sqrt{2D_L t}, \ \sigma_T = \sqrt{4D_T t}. \tag{4.5}$$

The longitudinal diffusion D_L is reduced. In some gases, and in the case of DUNE's HPgTPC, the reduction of D_L helps in improving the drift time resolution [22]. Ideally in a TPC, a very strong localized signal is best. So a large diffusion in the detector will lower the resolution and make it more difficult to extrapolate data.

4.3 Electron Drift

In the absence of an electric field, the dominant process of the detector is ionization then reattachment. In the presence of an E-field, however, the electrons are forced away from their original atoms[4] diffusing out and drifting up the electric field to the anode wires at constant speed. In this scenario, which is necessary for particle detection, electron drift can be modeled by kinetic gas theory. Townsend found the drift velocity to be

$$v = \frac{keE\tau}{m}, \tag{4.6}$$

where τ is the average collision time, m the mass of drifting electrons, and k is a constant dependent on assumptions of energy distribution of electrons. This is a simple formulation as v and τ will depend on gas properties [22].

---

[4] They can be attached to other atoms see Section 4.4.

When a B-field is added to the detector in an orthogonal direction to the E-field, the effect is a reduction in drift velocity and a reduction in the transverse diffusion. This is expressed as:

$$v_b = \frac{E}{B} \sin \theta_B = \frac{E\omega\tau}{B\sqrt{1 + (\omega\tau)^2}}, \tag{4.7}$$

where θ_B is the angle between the drifting swarm and the electric field in the plane perpendicular to $\vec{B}$, $\omega = \frac{EB}{m}$ is the Larmor frequency, τ is the mean collision time, $\omega\tau = \tan\theta_B$, and [22]. For the DUNE HPgTPC, however, the B-field will be parallel to the E-field. Under these conditions, we expect that the drift velocity is equivalent to that of no magnetic field $v_b = v_0$, the longitudinal diffusion to not change $\sigma_L = \sigma_0$, but the transverse diffusion to be reduced [22]:

$$\sigma_T = \frac{\sigma_0}{\sqrt{1 + \omega^2\tau^2}}. \tag{4.8}$$

When the magnetic field is neither perpendicular nor parallel to the E-field, the drift can be modeled by:

$$\vec{v} = \frac{e\tau}{m(1 + (\omega\tau)^2)} \left[\vec{E} + \omega\tau \frac{\vec{E} \times \vec{B}}{B} + (\omega\tau)^2 \frac{\vec{B}(\vec{E} \cdot \vec{B})}{B^2} \right]. \tag{4.9}$$

Even though DUNE will implement a magnetic field parallel to the electric field, there will be edge effects where the magnetic field and electric field are not nicely aligned. In the regions, electrons will be lead astray away from the readout planes. However, these regions are few and small. DUNE will also work to minimize these affects as much as possible. Sometimes, however, the drifting electrons are not able to make it to the readout planes as they recombine with electro-negative contaminants.

4.4   Electron Attachment

If electro-negative pollutants are allowed in the gas mixture, there will be some non-zero probability of attachment per collision h [22]. Given the number of collision per unit time, the average time to attachment is then $(hN)^{-1}$. The number of collisions per unit drift

length is then given by $\frac{h}{v\tau} = \frac{heE}{mv^2}$. This leads then to the electron loss in a drift length x:

$$dn = -\frac{eE}{mv^2}dx. \qquad (4.10)$$

Then the number of surviving electrons after a drift length s is described by:

$$n(s) = n_0 e^{\frac{-heE_s}{mv^2}} = n_0 e^{-\frac{s}{\ell}}. \qquad (4.11)$$

Here ℓ is the mean capture length. Then we can find the average collected charge normalized initial ionization to be:

$$\frac{Q_S}{Q_0} = \int_0^s e^{\frac{-ps'}{\ell}}ds' = \frac{\ell}{p}(1 - e^{\frac{-ps}{\ell}}), \qquad (4.12)$$

where p is the percentage of contaminant added [22]. The primary electrons that survive attachment are not able to provide a sufficiently large signal to be detected. All is not lost, however, as the electrons will multiply and create an avalanche as they near the readout plane, providing a recognizable signal.

4.5   Electron Avalanche and Readout

As the primary ionized electrons drift towards the anode wire, they pass through a gating-grid at which point the voltage is increased and the electrons accelerate. In this acceleration region, the electrons can gain sufficient energy to ionize atoms or molecules. These secondary electrons also begin to accelerate towards the anode and will ionize more electrons which, in turn, accelerate and ionize more electrons and so on, creating an 'electron avalanche.' Given that electrons are more mobile than their ion counterparts, the avalanche takes   the   form   of   a   tear   drop-like   shape   as   shown   in   Figure   4.3. Another process that important to the signal readout is Penning transfer. Penning transfer occurs when an excited atom or molecule has enough energy to ionize another atom or molecule of a different species [23].

The probability of ionization per unit length
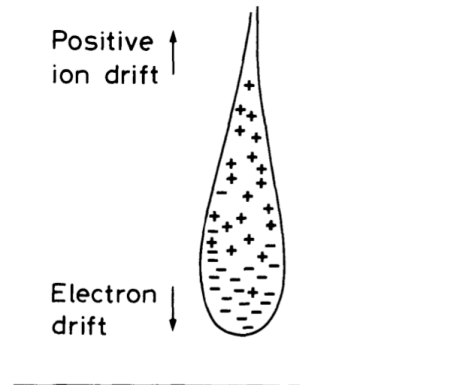
given by[5] $\alpha = \frac{1}{\lambda}$ is the Townsend coefficient and the number of electrons in a path dx is

$$dn = n\alpha dx. \qquad (4.13)$$

A simple integration yields the total number of electrons created due to the avalanche after a distance x yields

$$n(x) = n_0 e^{\alpha x}, \qquad (4.14)$$

where n_0 is the initial number of freed electrons. The signal gain is then

$$G = \frac{n}{n_0} = e^{\alpha x}. \qquad (4.15)$$

This is a fortunate solution to detecting primary electrons [21]. All that was required was a large enough voltage at the readout plane causing the electrons to accelerate and gain energy.

Now that the time projection chamber technology has been explained, how will this be implemented at DUNE? As discussed in Chapter 3, DUNE will use liquid argon time projection chambers for its far detector modules and for one of the detectors in the near detector hall. A gaseous argon TPC will also be employed in the ND hall following the liquid argon TPC.

4.6   DUNE's HPgTPC

One of DUNE's TPCs will be a high pressure TPC with a gaseous argon and methane medium, specifically the gas mixture will be 90% argon and 10% CH_4 (this mixture is commonly known as P-10). The design of which is based on the ALICE experiment's TPC as show in Figure 4.4. The ALICE TPC has an outer radius of about $2.5\,\mathrm{m}$ and a length of about $5\,\mathrm{m}$. It was operated at atmospheric pressure, a voltage of $400\,\frac{\mathrm{V}}{\mathrm{cm}}$, and used a gas

---

[5] λ the mean free path as in Section 4.2.

mixture of neon, carbon dioxide, and nitrogen [24].

Argon is chosen as the target nucleus for neutrino interactions and has the added benefits of being relatively inexpensive and a noble gas. This means that electron attachment (and therefore loss in signal) can be reduced. The added methane is a quencher gas. This
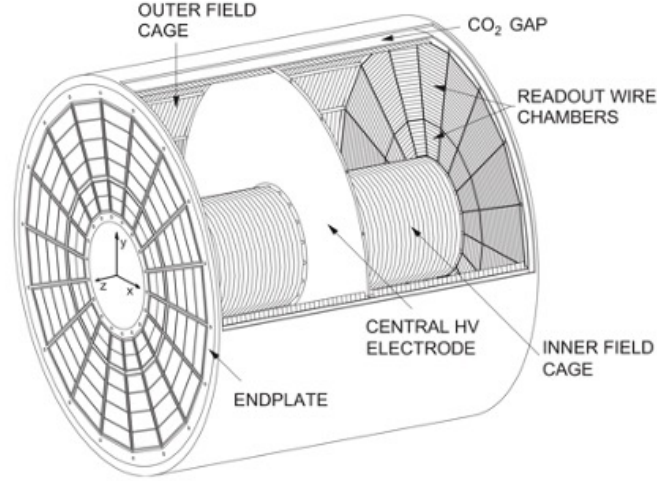

Figure 4.4: The TPC from the ALICE experiment at CERN. The HPgTPC design will follow the ALICE specifications. Retrieved from [24].

name is given to methane because it 'quenches' photons released from argon. If an argon atom gains energy and enters an excited state (This can happen if the atom is not ionized) it will eventually release that energy as a photon in order to return to its ground state. These photons could cause all sorts of ionization and greatly impact the readout signal, however, methane is introduced to absorb the photons as it has a lower energy state resonant with these photons [25].

Now with the discussion of neutrinos, DUNE, and particle detection concluded, this thesis will turn to studies conducted on the drift properties and the impact on track reconstruction in the DUNE's HPgTPC.

Chapter 5

Simulation Tools

As DUNE has not yet to finish construction and begin observing neutrino events, the work presented in this thesis was done through simulation. There are two studies each of which had different simulations. Investigation of drift properties in DUNE's HPgTPC uses the PyBoltz simulation code. Drift properties impact on track reconstruction efficiency which uses the GArSoft simulation code.

5.1   PyBoltz

PyBoltz is a Monte-Carlo simulation code developed by a team at University of Texas at Arlington [26]. It is a translation from the MagBoltz simulation code [27] developed for the ease of use in Python. The code simulates electron drift properties based on a given gas mixture. This is vital information for experiments using time projection chambers, drift chambers, and multiwire or micropattern proportional chambers to detect particles [26].

In order to perform the track reconstruction, details of the electron's drift velocity, diffusion, attachment rate, and ionization rate (given the properties of the gas detector) must be known. These parameters matter because they affect the resolution of the signal and accuracy in reconstructing tracks. Here enters PyBoltz: the Python package simulates electrons in the gas detector and reports drift properties. These properties will then be used by the ND-GAr reconstruction software. Here is a full list of outputs from PyBoltz:

- Drift velocity $[\frac{mm}{\mu s}]$

- Transverse diffusion $[\frac{\mu m}{\sqrt{cm}}]$

- Transverse diffusion error [% error]

- Longitudinal diffusion $[\frac{\mu m}{\sqrt{cm}}]$

- Longitudinal diffusion error [% error]

- Attachment rate $[\frac{Attachments}{cm}]$

- Attachment rate error [% error]

- Ionization rate $[\frac{Ion\ pairs}{cm}]$

- Ionization rate error [% error]

- Mean collision time [ps]

As discussed in Chapter 4, the drift properties output by PyBoltz are dependent on the gas parameters. These parameters include both intrinsic properties of the gas such as: temperature, pressure, and composition of the gas, and external factors applied to the gas mixture: electric and magnetic fields.

5.2   GArSoft

GArSoft is a simulation software developed by a team at Fermilab [28]. It runs a Monte-Carlo simulation of n particles (chosen by the user) in the detector given some initial data and then simulates tracks, the energy deposited into the detector, the electronics readout, and performs reconstruction. Relevant to the studies presented in this thesis, the initial data GArSoft pulls from includes:

- starting position (x, y, z) and spread in each $(\sigma x, \sigma y, \sigma z)$ [cm],

- starting angle θ in the YZ and XY planes and spread in each $(\sigma \theta_{YZ}, \sigma \theta_{XY})$ [degrees],

- starting momentum (p) and spread in momentum (σp) [GeV],

- other properties of the detector including drift properties and conditions of the detector,

where the spread in values can be Gaussian or uniformly distributed. The output of GArSoft can be analyzed to understand how well the reconstruction was performed.

Chapter 6

Drift Properties for the HPgTPC

Presented here are findings from a study done varying conditions of the HPgTPC in order to understand the impact on the electron drift properties. This chapter concludes with a look into the tolerance of variations in drift the drift velocity.

6.1 HPgTPC Nominal Conditions

HPgTPC Control	
Parameter	Value
Electric Field	$400\,\frac{V}{cm}$
Pressure	10 bar
Temperature	23° C
Gas Mixture	P-10

Table 6.1: Describes the nominal assumptions about DUNE's HPgTPC.

DUNE's HPgTPC will follow the specifications voltage specification of the ALICE TPC, but will be run at 10 bar. The TPC will have a gas P-10 gas mixture.[1] For the studies here, the base temperature will be 23° C. These parameters, summarized in Table 6.1, puts the electron drift velocity in the region of $\sim 30\frac{mm}{\mu s}$ as can be seen in Figure 6.1. With a control defined, the following sections will explore variations of these conditions.

---

[1] Recall this is a combination of 90% Argon and 10% Methane.
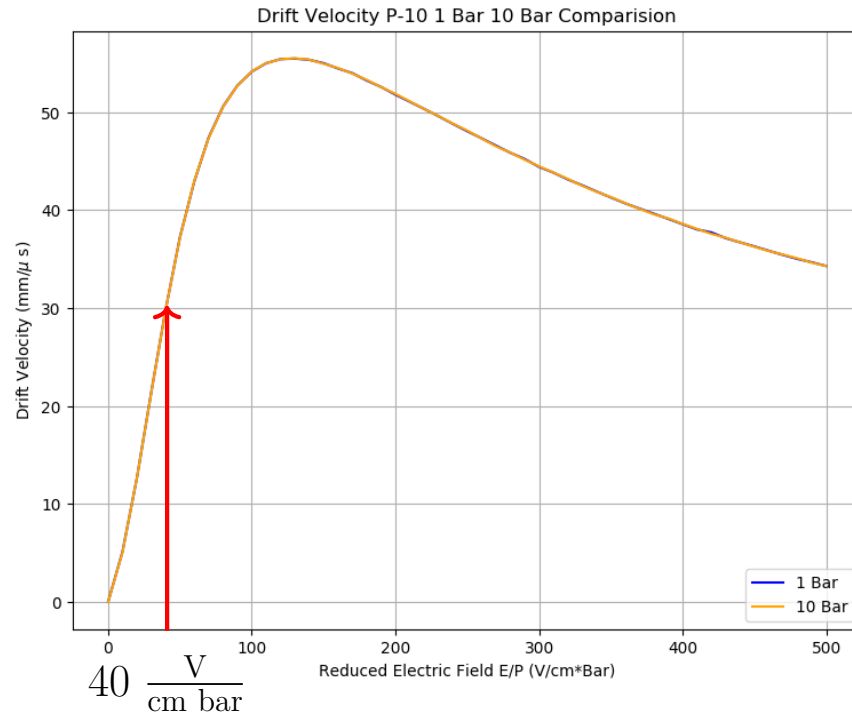
Figure 6.1: The electron drift as a function of E/P at 1 bar and 10 bar, since it is normalized the 1 bar and 10 bar curves align nicely. The HPgTPC will be run at $40 \ \frac{\mathrm{V}}{\mathrm{cm \ bar}}$, for P-10 mixture puts the drift velocity in the region of $30 \ \frac{\mathrm{mm}}{\mu \mathrm{s}}$.
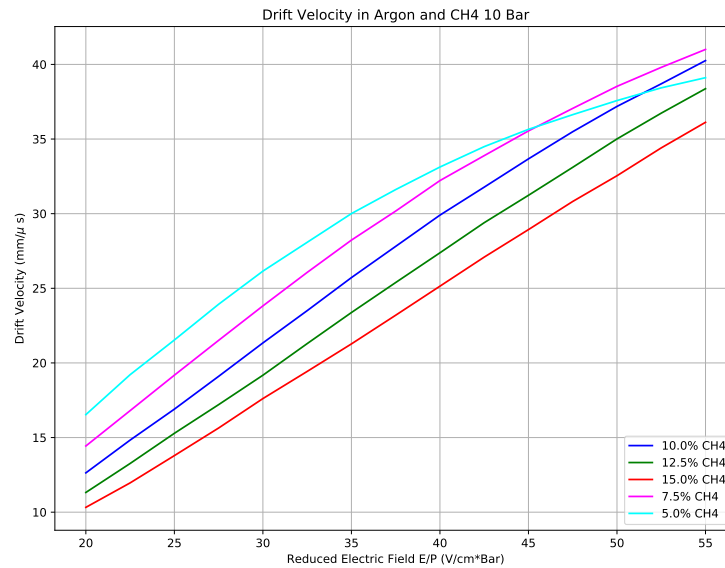
Figure 6.2: Lowering the CH_4 content will increase the electron drift velocity.

6.1.1   Altering Methane Content

Methane is added to the mixture as a quencher gas to help reduce and limit electron avalanches caused by photons (as discussed in Chapter 4). There is potential for the DUNE collaboration to lower the methane content due to safety concerns. Should the collaboration decided to lower the methane content there will be a significant change in the drift velocity as shown in Figure 6.2. If the methane content is lowered it would most likely be changed to 5%. The higher percentage of methane is shown in Figure 6.2 for contrast. Another potential change the collaboration is considering is altering the central cathode in the HPgTPC.

6.1.2   Drift Chamber

The ND-GAr detector will use the inner and outer readout chambers from the ALICE TPC while also employing a similar geometry as the gas drift chamber situated next to the ND-LAr [24]. In the current set up, the 4.994 meter detector is split in half by a central cathode creating two sections each about 2.5 meters in length with two readout chambers, one at each end of the detector [24]. There is potential in changing the HPgTPC drift chamber such that the central cathode gets pushed to one end of the detector with only one readout chamber at the other end. In this case the electron maximum drift length doubles from 2.5 to 5 meters. This change might alter the applied electric field to the TPC from $400 \frac{V}{cm}$ to $200 \frac{V}{cm}$. In this case there is a significant change in drift velocity, transverse, and longitudinal diffusion coefficients as can be seen in Figures 6.3, 6.4, and 6.5. The drift velocity reduces by over half from $\sim 30 \frac{mm}{\mu s}$ to $\sim 12.6 \frac{mm}{\mu s}$.
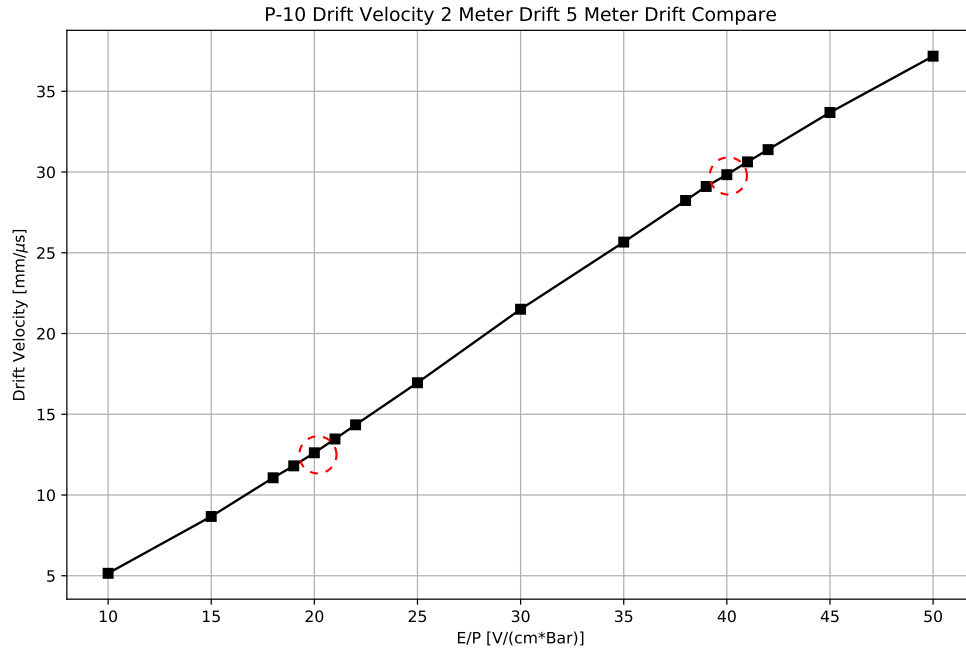
Figure 6.3: Moving the central cathode to create a maximum drift distance of 5 meters will reduce the drift velocity by more than 1/2.

6.2   Temperature

Adjusting the temperature in the HPgTPC will cause a noticeable shift in the electron drift velocity. Figure 6.6 shows the standard 23° C and two extremes of 19 and 27° C. It is also clear to see that an increase in temperature results in an increase in drift velocity. In the case of a drift length of 2 meters this would imply 67.7 μs and 66.1 μs drift time for the two extremes of 19 and 27° C respectively. This difference of 1.6 μs at an assumed velocity of 30 $\frac{mm}{\mu s}$ implies a separation of 48 mm of the detected charge. This spread will lower the resolution and negatively impact the reconstruction ability.
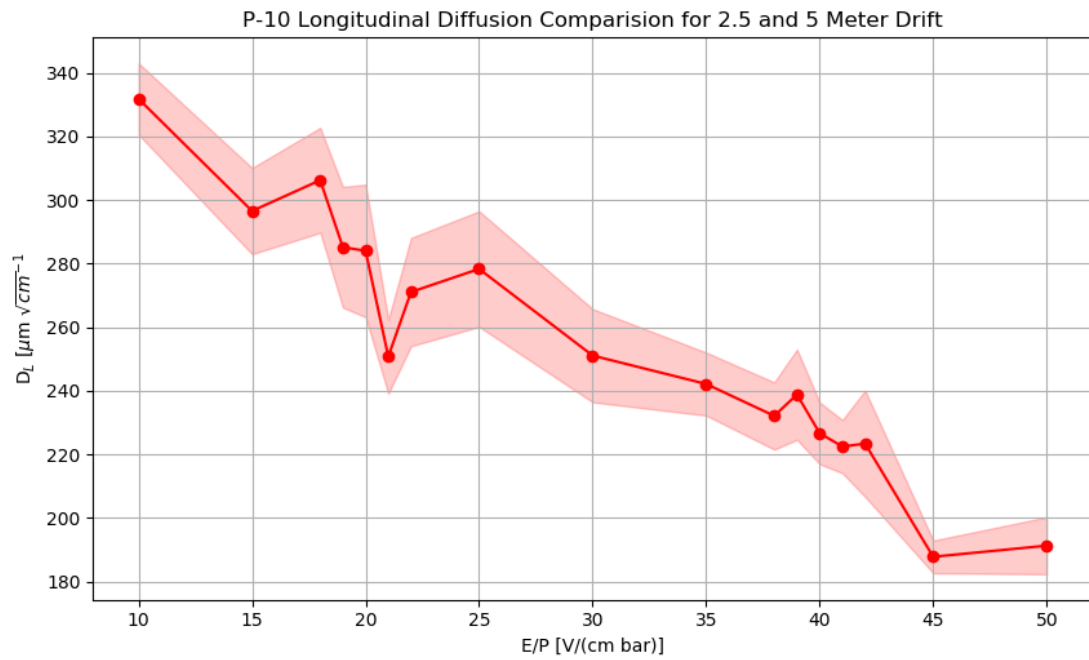
Figure 6.4: The longitudinal diffusion at E/P of 20 compared to 40.
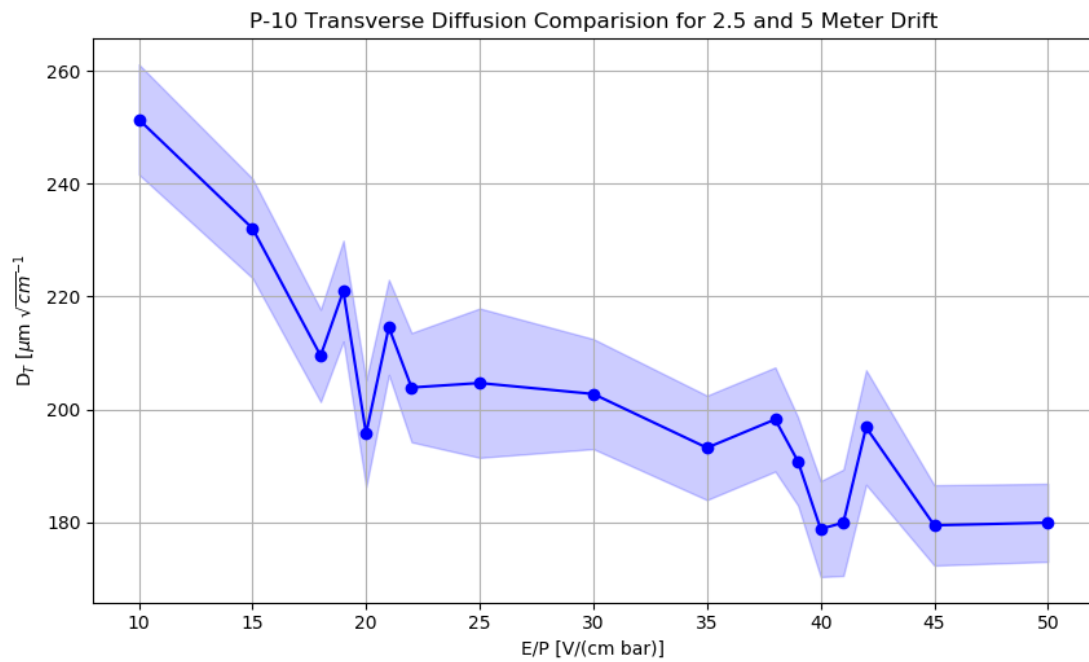
Figure 6.5: The transverse diffusion at E/P of 20 compared to 40.
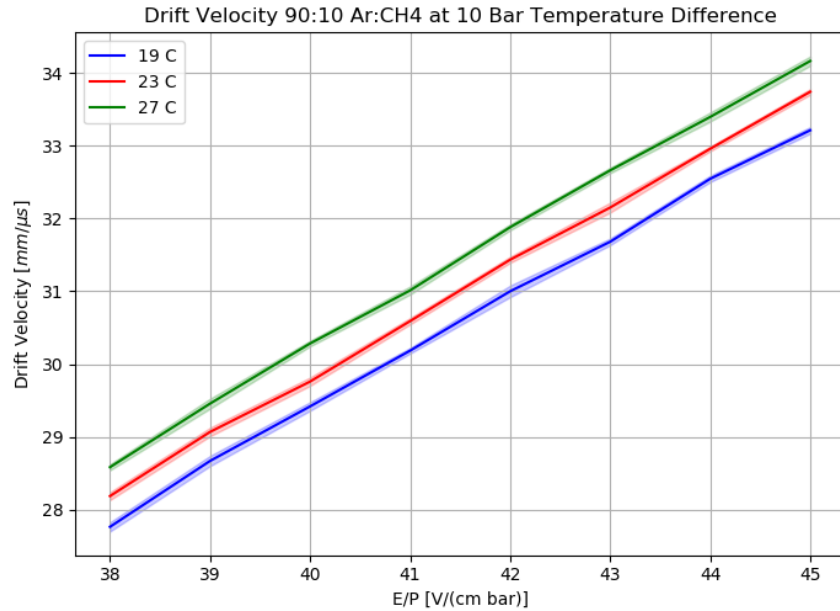
Figure 6.6: The electron drift velocity as a function of reduced electric field. Increasing the temperature increases the drift velocity.

6.3   Magnetic Field

One of the key aspects to the HPgTPC is its magnetic field. The HPgTPC will have a superconducting magnet coil that will supply half of a Tesla aligned with the electric field. As mentioned in Chapter 4, there will be small regions where the magnetic field will not perfectly overlay with the electric field. In these regions the drift velocity will in general have three nonzero components, compared to when the magnetic field is aligned with the electric field. In that case there is in general only one nonzero component[2]. It is very important to understand how the electron drift will be altered in these regions. Currently PyBoltz cannot simulate off-axis magnetic fields. When looking at the regions where magnetic and electric fields line up (as desired) we expect the drift velocity to be unaffected by the addition of a magnetic field and PyBoltz confirms this. The magnetic field will, however, cause a reduction

---

[2]   In the direction of the E-Field.

in the transverse diffusion:

$$\sigma_T = \frac{\sigma_0}{\sqrt{1 + \omega^2 \tau^2}} \tag{6.1}$$

as in [22]. The transverse diffusion σ_0 in the absence of magnets, and ω and τ are the Larmor frequency and mean collision time as described in Chapter 4. This effect is better observed at lower pressure as shown in Figures 6.7 and 6.8.

6.4   Ionization Region

As discussed in Chapter 4, Penning transfer is an important process in the ionization region and this process accounts for a noticeable increase of the detector's signal gain. As the drifting electrons near the readout plane at the ends of the HPgTPC they accelerate and can ionize secondary electrons. This process is known as an electron avalanche and helps in giving a readable signal from the detector. Figures 6.9 and 6.10 show PyBoltz simulation results of the Townsend coefficients for the HPgTPC as the the electric field gets larger. Enabling Penning transfer in the gas[3] shifts the initial jump from zero up 1000: a significant change of the signal gain.

6.5   Attachment

When electro-negative contaminants, such as O_2, Cl, H_2O, and CO_2, are included in the gas mixture there is significant potential of signal loss due to electron capture. Naturally electrons reaching the readout plane is a crucial process for track reconstruction. For track reconstructions this information lies in the electron lifetime. Given a drift velocity, v, and a drift length, ℓ, the drift time $t = \frac{\ell}{v}$. Let N_0 be the initial number of liberated electrons then the ratio of number of electrons that survive, N_e, to N_0 as a function of the electron lifetime τ is

$$\frac{N_e}{N_0} = e^{-\frac{\ell}{v\tau}}. \tag{6.2}$$
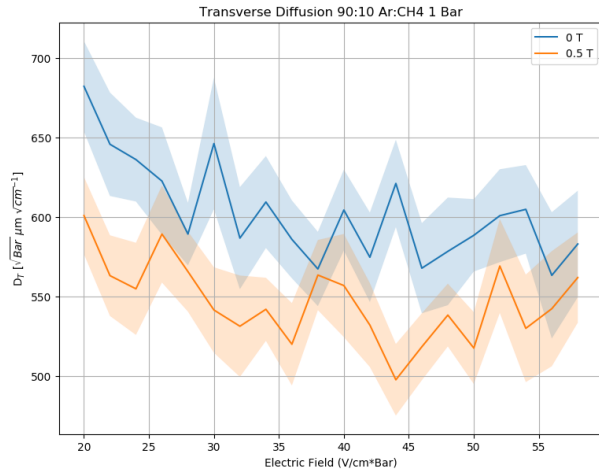
---

[3]   See Appendix A.

Figure 6.7: The transverse diffusion coefficient as a function of reduced electric field. At lower pressure the effect of reduced transverse diffusion is visible.
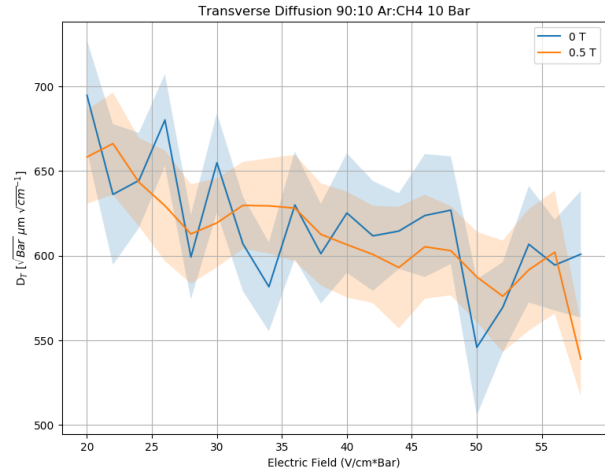

Figure 6.8: The transverse diffusion coefficient as a function of reduced electric field. Increased pressure suppresses the observed effect in transverse diffusion caused by applying a B-field.
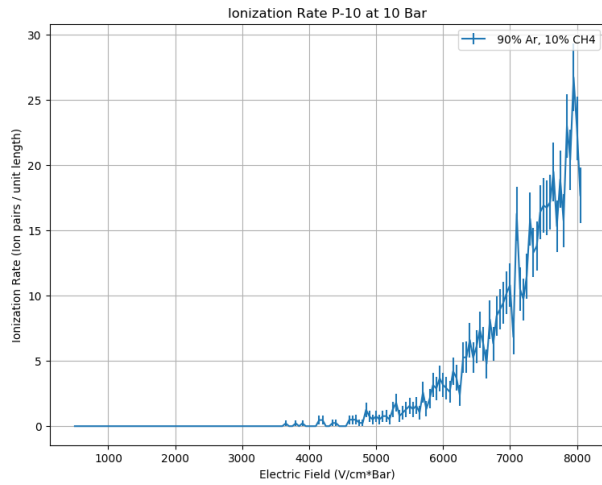

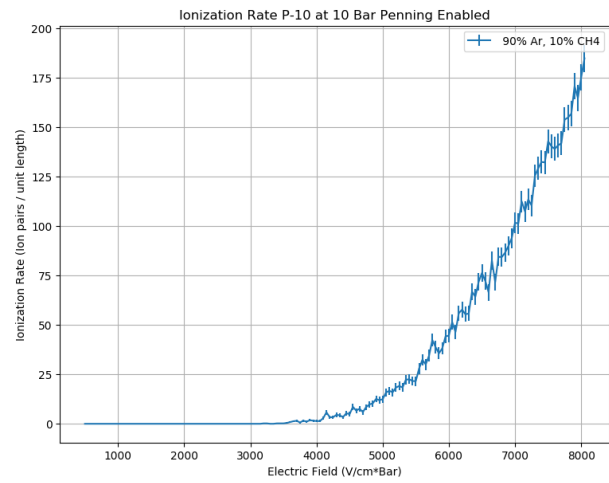Figure 6.9: The ionization rate in P-10 without Penning transfer.

Figure 6.10: The ionization rate in P-10 with Penning transfer.

Ratios for a drift length of 50, 250, and 500 cm is show in Figure 6.11. For the DUNE HPgTPC oxygen gas is entering the detector is of main concern and so here too.
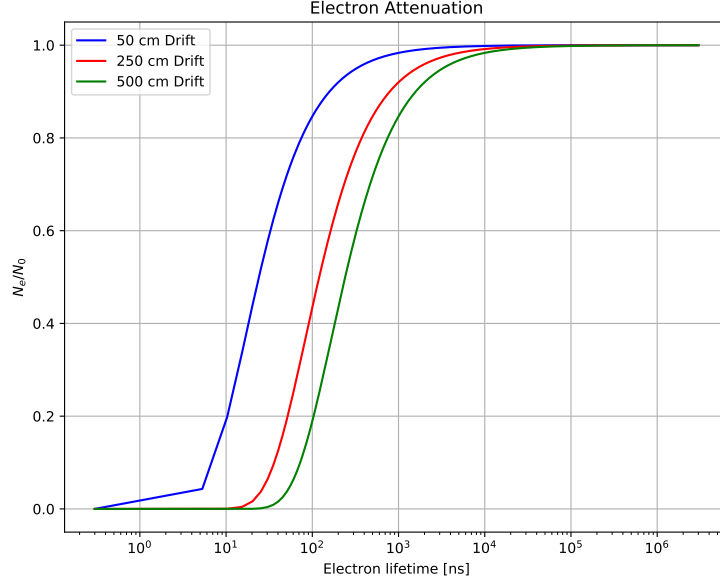
Figure 6.11: Ratio of survived to liberated electrons as a function of electron lifetime for a 50, 250, and 500 cm drift.

When running initial PyBoltz simulations it appeared as though even a few parts per million of an electro-negative contaminant involving oxygen will destroy the detector's signal as shown in Figure 6.12. These results are suspicious and prompted further investigation of PyBoltz[4] attachment.[5]

This issue has been identified as an incorrect scaling factor for 3-body attachments in the code. By default the code is based on a pure oxygen mixture which explains why the discrepancy in simulated attachment is worse for mixtures that contain less and less oxygen. For argon-oxygen mixtures this scaling factor needs to be set to 0.02 as advised from the MagBoltz author [29]. Making this adjustment greatly reduces the simulated attachment

---

[4]   Since PyBoltz is a translation of MagBoltz to Python the problem persists in MagBoltz as well.

[5]   See Appendix B for an in depth discussion of the discrepancy in PyBoltz and MagBoltz attachment.

discrepancy as can be seen in Figure B.10. The reassessment of attachment in the HPgTPC is shown in Figure 6.13. With this modification it is now possible to have oxygen contamination at the level of part per million and still retrieve a detectable signal.
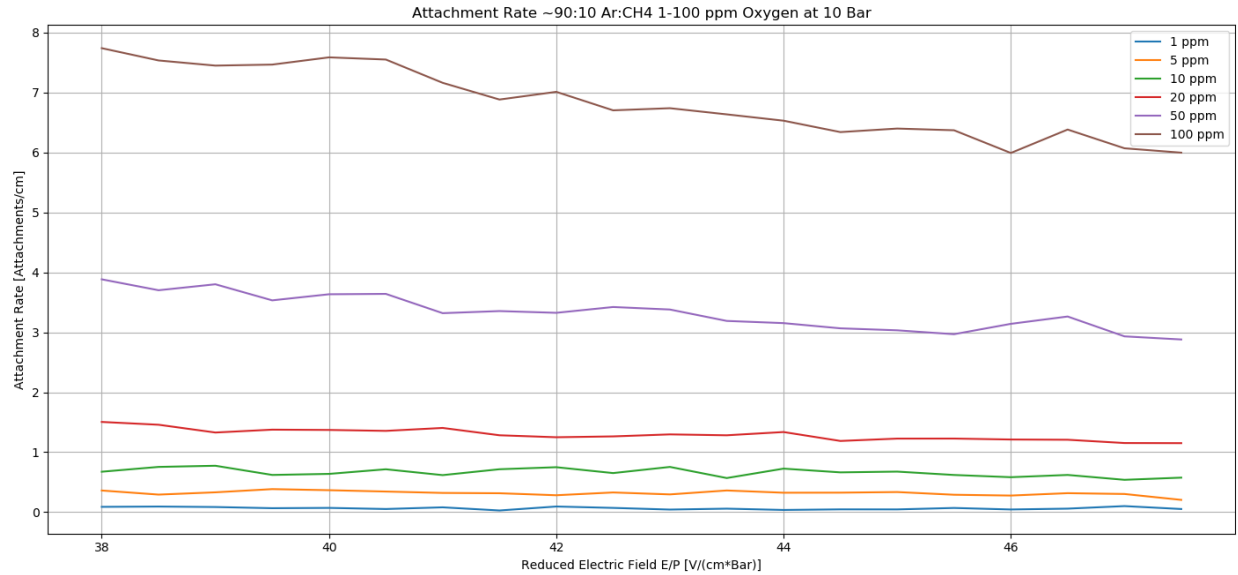

Figure 6.12: PyBoltz simulated attachment rate in P-10 plus 1-100 parts per million of oxygen added. Attachment values appear larger than expected, simulated with default 3-body scaling factor of 1.0.
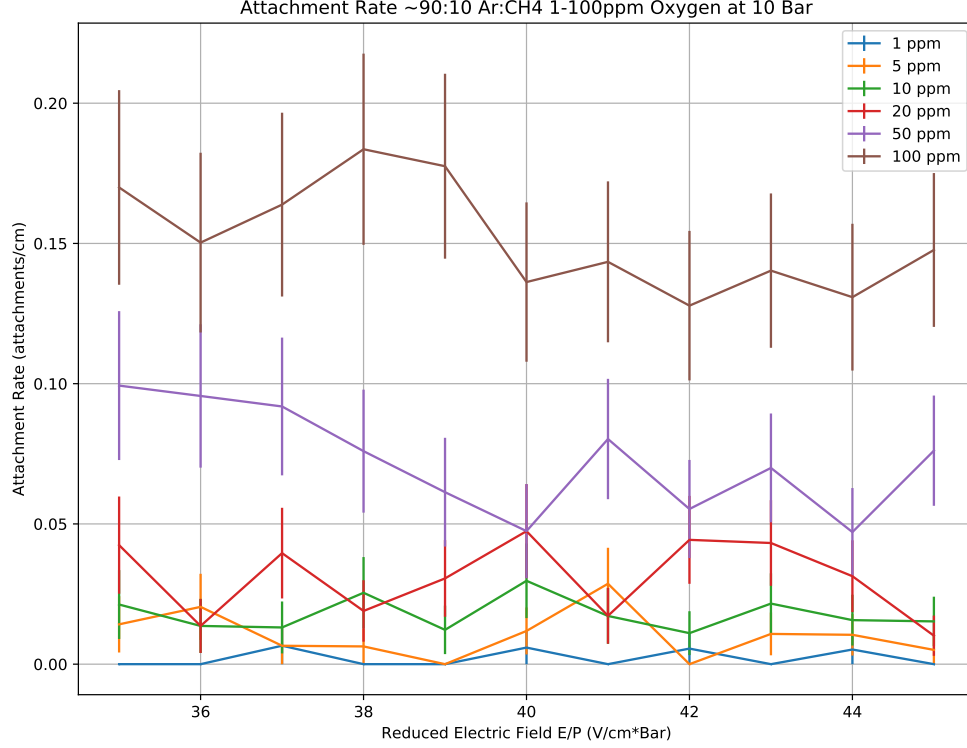
Figure 6.13: PyBoltz simulated attachment in P-10 plus 1-100 parts per million of oxygen with adjusted 3-body attachment scaling factor of 0.02.

6.6   TPC Requirements

TPC Operation Region			
Parameter	Base Drift Velocity $\left[\frac{mm}{\mu s}\right]$	Minimum	Maximum
E-Field	29.847	396 $\left[\frac{V}{cm}\right]$	404 $\left[\frac{V}{cm}\right]$
Pressure	29.799	9.9 [Bar]	10.1 [Bar]
Temperature	29.832	20.8° C	25.4° C

Table 6.2: HPgTPC requirements to stabilize the electron drift velocity at $\sim 30 \frac{mm}{\mu s} \pm 1\%$

On any given side of the gaseous TPC is the ECAL. As previously mentioned, this is a crucial component as it measures the energy and position of charged particles that passed through the TPC. Electrons and photons will shower in the ECAL allowing their reconstruction and identification [20]. Given that the ECAL is composed of 2×2 cm^2 tiles, we must control the drift velocity to an error of 1%. Figures 6.14, 6.15, and 6.16 show the
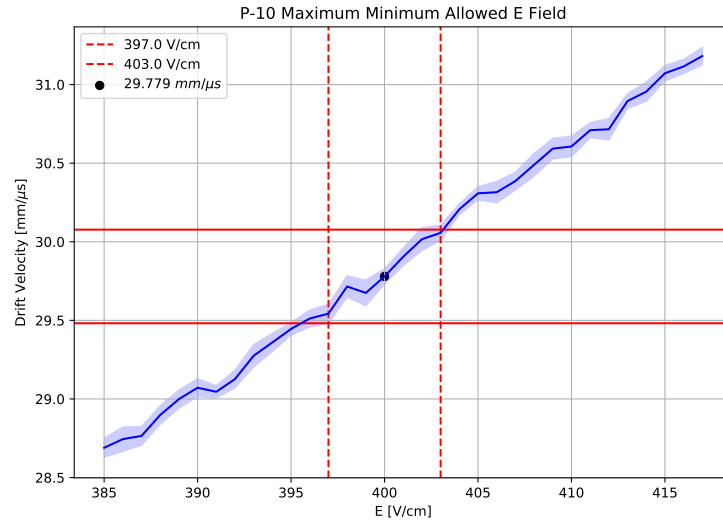
Figure 6.14: The electron drift velocity as a function of electric field. The horizontal red bars give 1% error on the assumed drift velocity at 400 Volts/cm (29.847 mm/μs).

allowed range of applied electric field, pressure, and temperature of the HPgTPC respectively.
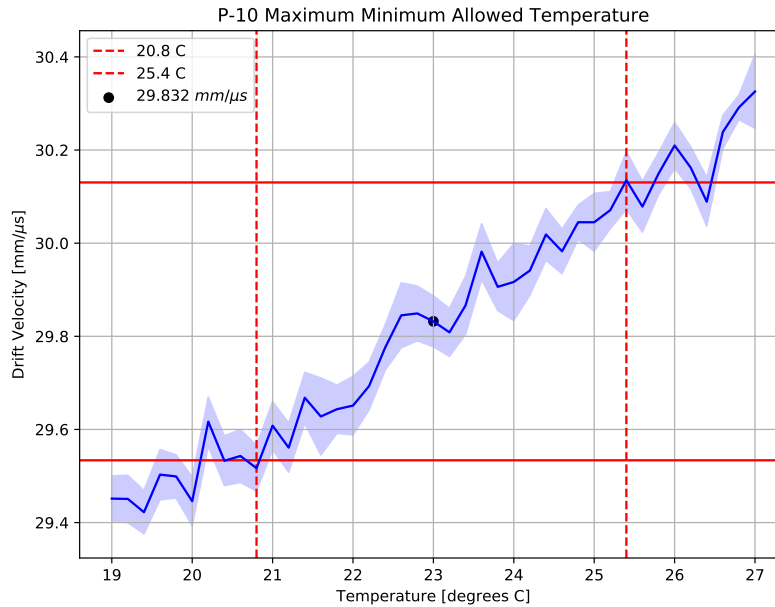
These results are also summarized in Table 6.2.

Figure 6.16: The electron drift velocity as a function of temperature. The horizontal red bars give 1% error on the assumed drift velocity at 23 ° C (29.832 mm/μs).
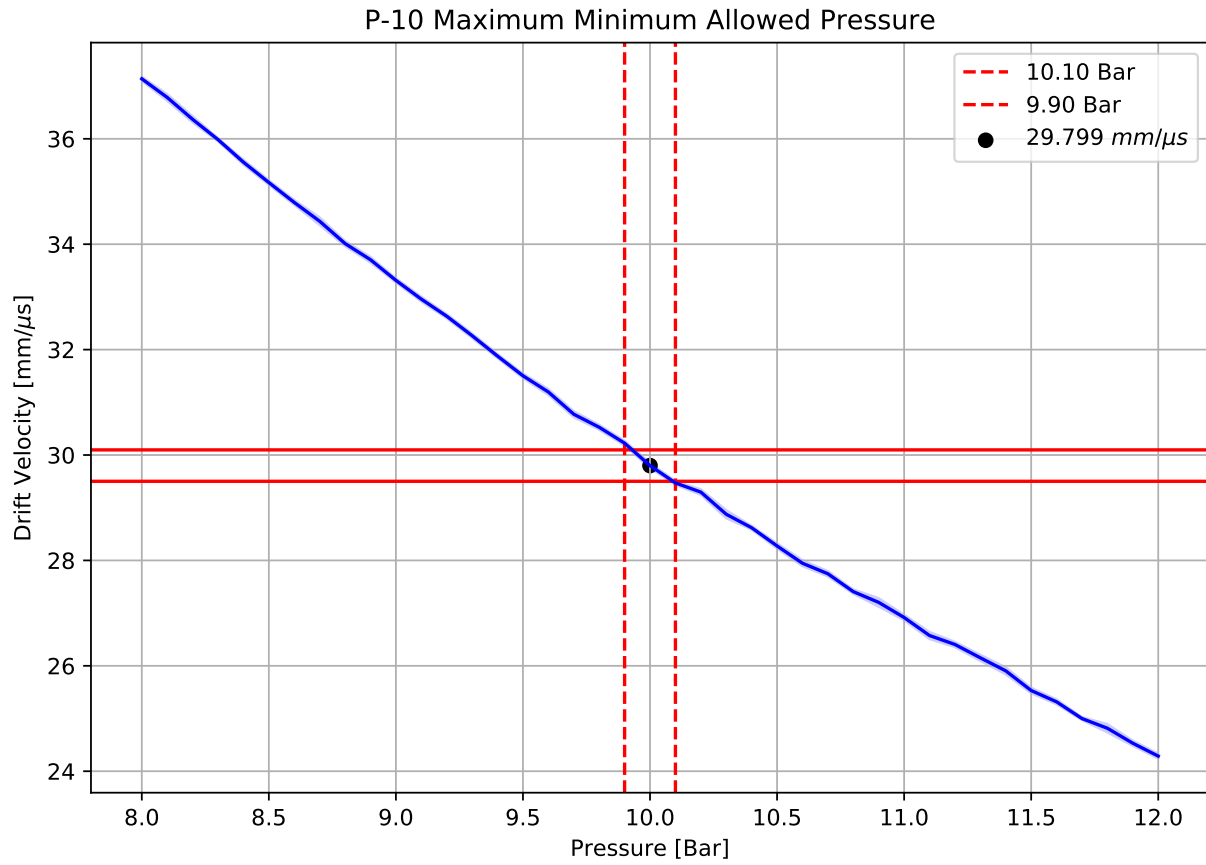
Figure 6.15: The electron drift velocity as a function of pressure. The horizontal red bars give 1% error on the assumed drift velocity at 10 Bar (29.799 mm/μs).

6.7   Summary

In this chapter the standard conditions of DUNE's HPgTPC have been described, then results of changing these conditions was examined, and concluded by describing the allowed regions of operation for the HPgTPC. PyBoltz is not yet able to simulate electron drift properties in the special regions of the HPgTPC where the angle between the magnetic field and electric field are nonzero but matches the expected results when the fields are parallel. The default simulation overestimates electron attachment in the detector by about two orders of magnitude for argon mixtures. To meet the stability requirements of the drift velocity at $\sim$30 $\frac{mm}{\mu s}$ the HPgTPC should be held at a pressure between 9.9 and 10.1 Bar, 20.8 and 25.4 degrees Celsius, and the electric field kept between 396 and 404 $\frac{V}{cm}$.

Chapter 7

Track Reconstruction Efficiency

Presented in this chapter are findings from an investigation of diffusion on track reconstruction efficiency. As mentioned in Chapter 5, GArSoft simulates particles in the detector then reconstructs their tracks as shown in an 'event display' like Figure 7.1. The event display shown in Figure 7.1 illustrates GArSoft's reconstruction of an initial muon neutrino event. The incoming neutrino interacts and several particles are created. The neutrino interaction produces a muon and a proton which then produce pions (a π^+ and a π^0), gammas, and many electrons.
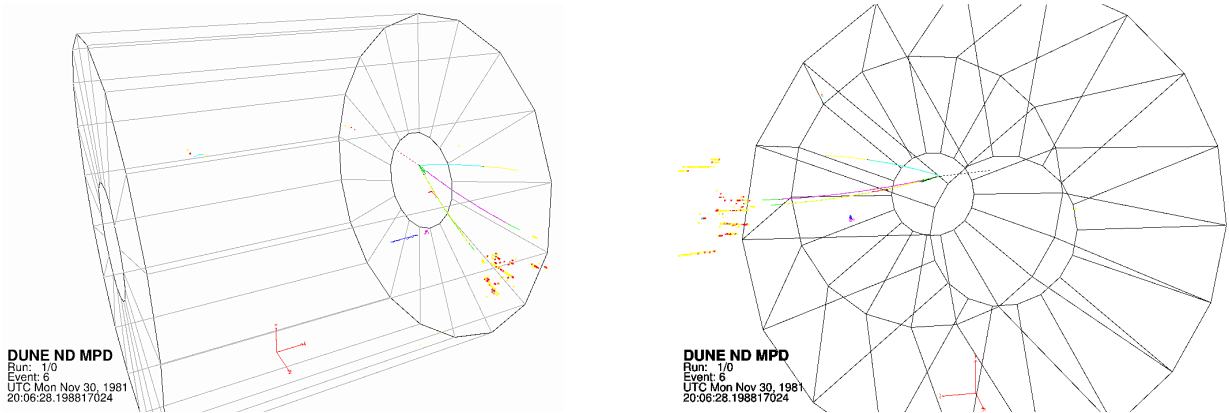

Figure 7.1: A muon neutrino enters the TPC (dashed line), the interaction to produces a μ^- (cyan), p^+ (pink/red), π^+ (green/yellow), π^0 (neutral particle, track not shown), and those create other electrons (other colors/tracks).

Particles produced from interactions in the ND-LAr will pass through the HPgTPC and their tracks will be reconstructed as well as potential tracks created from interactions

on the argon gas. Muons and protons among these will be reconstructed. The main study done here is of muons. A simple study of track reconstruction efficiency for protons was done as well. As before with the PyBoltz simulations some nominal base case needs to be put forward in order to understand deviations in the study.
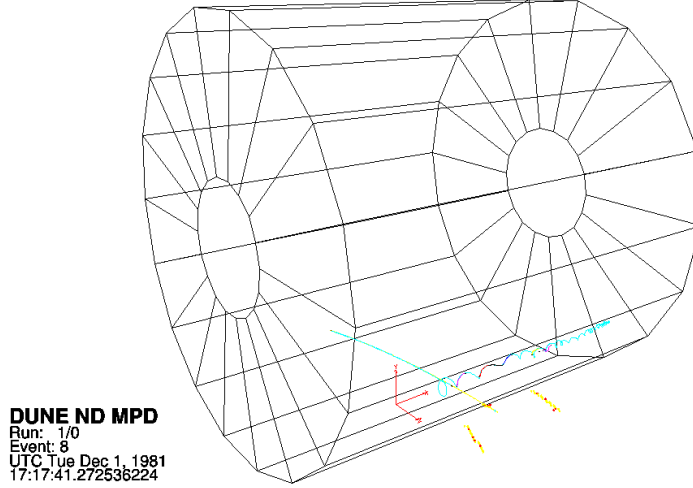

Figure 7.2: Muon passes through HPgTPC and kicks out electron that drifts to the readout plane.

7.1   The Nominal Setup: μ^-

Muons exiting the ND-LAr are of primary concern for the HPgTPC, as such, the studies done here focus on reconstructing muons. An example reconstructed muon event is shown in Figure 7.2. For the present study, tracks were simulated uniformly throughout the detector and with a uniform spread in momentum. The x, y, z coordinates for the center of the detector is set to be $\langle 0, 0, 0 \rangle$. The neutrino beam travels in the $\hat{z}$ direction. The direction of electron drift through the detector is in the $\hat{x}$ direction. This leaves the $\hat{y}$ direction as the up-down direction. The simulation parameters are then: 100,000 muons simulated, a starting track positions from $\langle -250, -250, -250 \rangle$ to $\langle 250, 250, 250 \rangle$ cm, a drift velocity of 3.011 $\frac{cm}{\mu s}$, a momentum from .1 to 5 $\frac{GeV}{c}$, a temperature of 22.11° C, an angle, θ, in the YZ or XY planes from -20 to 20 degrees, a longitudinal diffusion of 201.25 $\frac{\mu m}{\sqrt{cm}}$, and a transverse

diffusion of 160.285 $\frac{\mu m}{\sqrt{cm}}$. With the Monte-Carlo (MC) simulation input data set an run, the simulation results can be analyzed to understand how the reconstruction performed. The results are shown in Figures 7.3, 7.4, 7.5, and 7.7.

In order to determine the track reconstruction efficiency, several steps are taken. First, for a MC simulated track there are x reconstructed tracks, where x could be zero. If there are reconstructed tracks then only those within 5 cm are selected. From there, if more than one reconstructed track was within 5 cm only the closest track to the true MC track is picked. This is called a matched track, it and the associated MC track are selected. This is done for every MC simulated track, and then the matched tracks are divided by the simulated tracks giving an efficiency plot like in Figure 7.7.
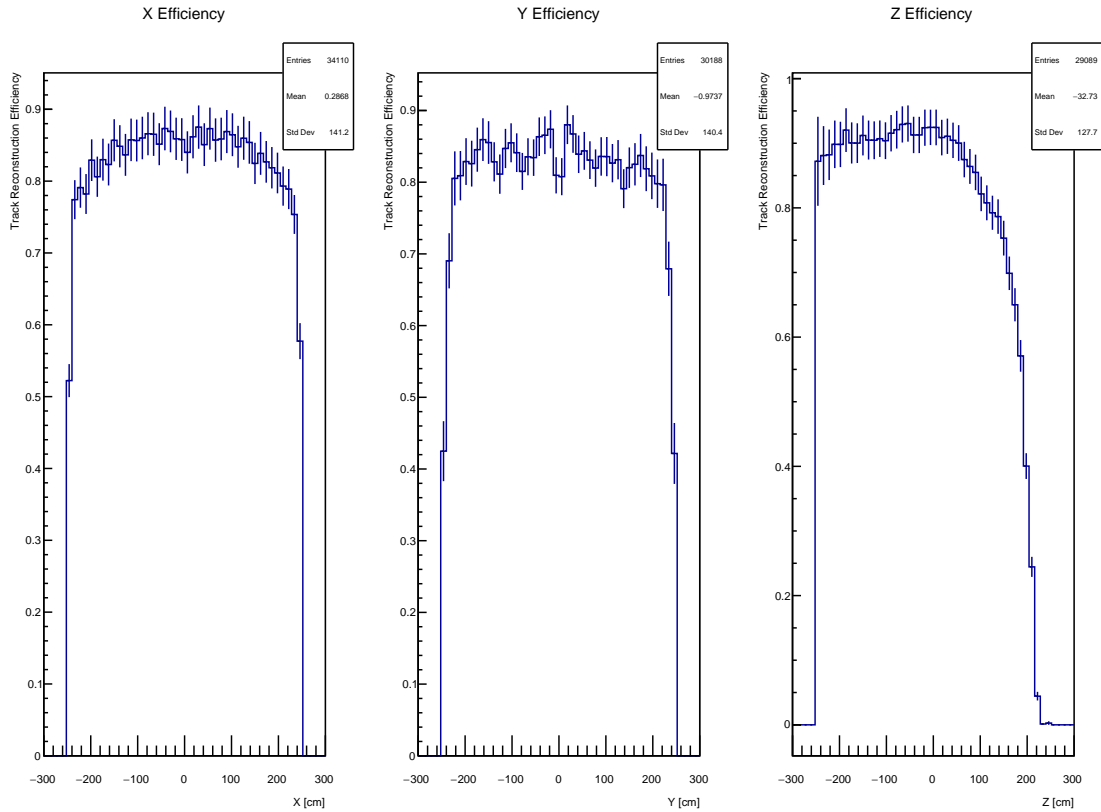

Figure 7.3: Track reconstruction efficiency in the $\hat{x}$, $\hat{y}$, and $\hat{z}$ directions for the nominal setup.

As another way to visualize how well the reconstruction software performed, the reconstructed track starting positions are shown next to the MC simulated track starting positions in the XY and YZ planes of the detector. For the nominal case this is shown in Figures 7.4 and 7.5. It is clear to see from these figures that the tracks have been reconstructed well. Note that for tracks starting farther along in $\hat{z}$, the direction of the neutrino beam, the efficiency drops off. These are tracks that start at the 'end' of the detector and exit and so they leave very short tracks. For the momentum, there is a noticeable drop in reconstruc-
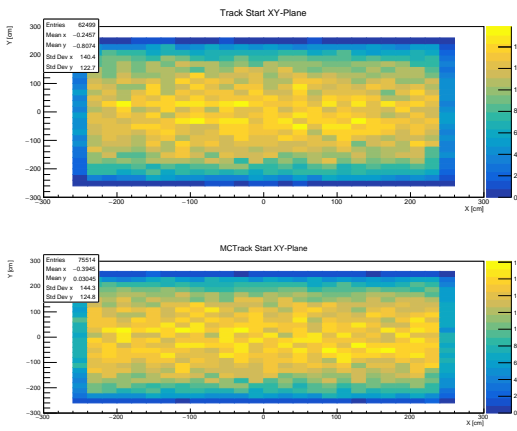

Figure 7.4: Reconstructed track (top) and MC simulated (bottom) track starting positions in the XY-plane for the nominal setup.
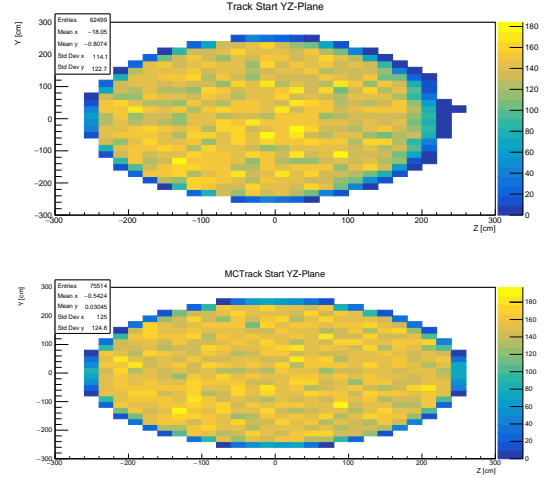

Figure 7.5: Reconstructed track (top) and MC simulated (bottom) track starting positions in the YZ-plane for the nominal setup.

tion ability at low momentum as shown in Figure 7.7. However, at higher momentum the efficiency is saturated at 80%. The momentum plots are consistent for this study and so have been omitted.

As can be seen in Figure 7.3, the reconstruction efficiency falls of for tracks starting at the ends of the detector. This loss in efficiency can be removed by considering only tracks in the fiducial volume of the detector. That is tracks are only included if the muons were simulated within a radius of 200 cm rather than 250 cm as described above. The resulting

reconstruction efficiency is shown in Figure 7.6. With this cut the reconstruction efficiency is boosted to about 95%. Furthermore it also helps improve the momentum reconstruction efficiency as shown in Figure 7.8, where the efficiency is saturated at 95% for tracks with more than 1 $\frac{\text{GeV}}{c}$.
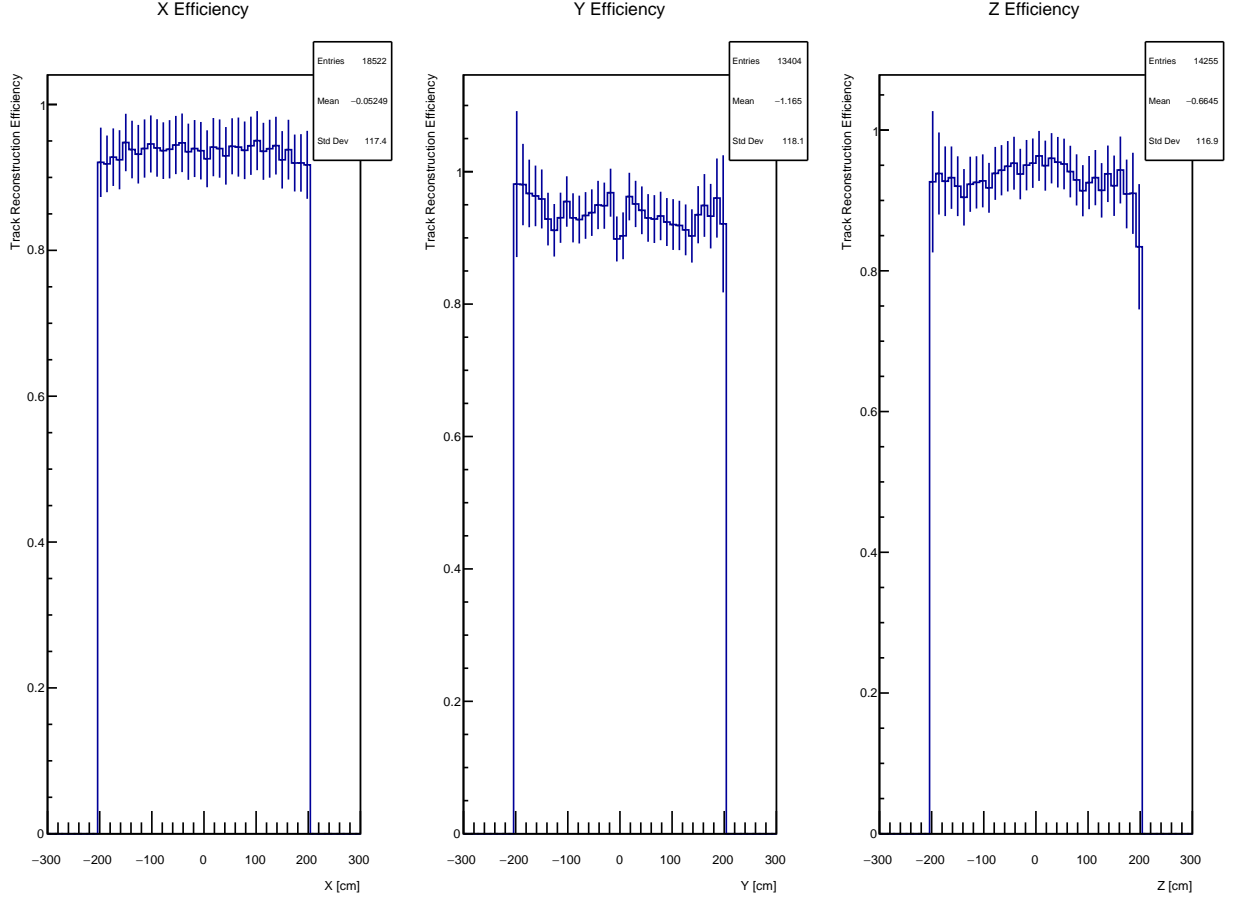

Figure 7.6: Track reconstruction efficiency in $\hat{x}$, $\hat{y}$, and $\hat{z}$ with tracks only in the fiducial volume of DUNE's HPgTPC.

7.2   Impact of Diffusion

The study done for this thesis was to understand how electron diffusion in the HPgTPC would impact GArSoft's ability to reconstruct the tracks. As shown above, in the case of
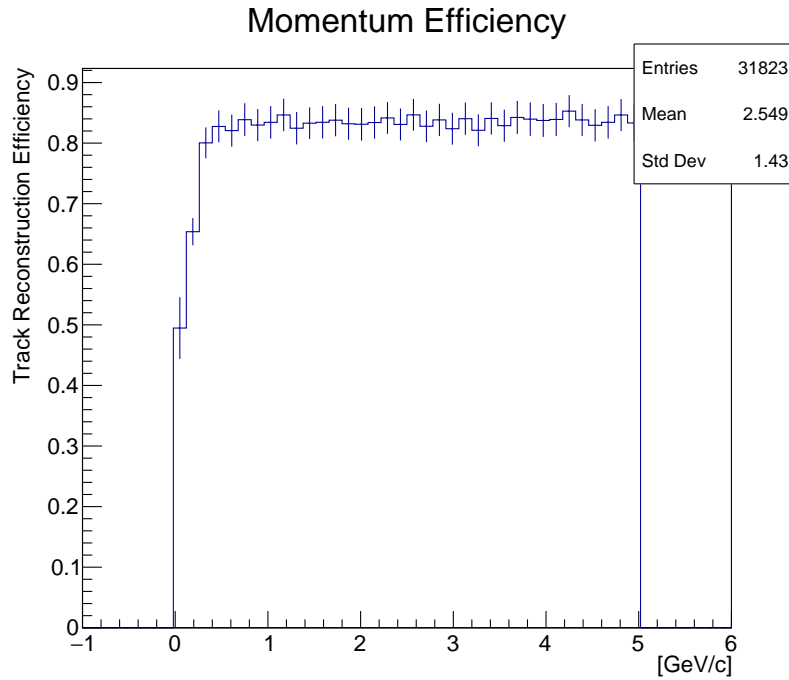
Momentum Efficiency

Entries	31823
Mean	2.549
Std Dev	1.43

Figure 7.7: Track reconstruction efficiency as a function of initial muon's momentum for the nominal setup.

Momentum Efficiency

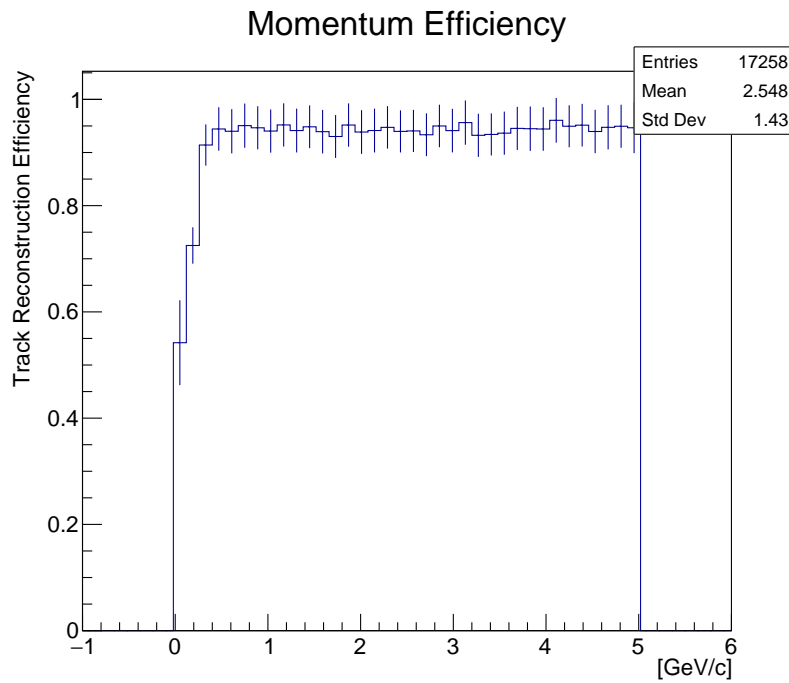| Entries | 17258 |
| Mean | 2.548 |
| Std Dev | 1.43 |

Figure 7.8: Reconstructed track momentum efficiency for tracks only in the fiducial volume of DUNE's HPgTPC.

the expected diffusion, GArSoft is able to perform the reconstruction well. The following sections will explore how this changes as the diffusion gets progressively worse in steps of two, four, ten, and twenty times the nominal diffusion constants.

7.2.1   2x Diffusion

The longitudinal and transverse diffusions are now set to 402.5 and 320.57 $\frac{\mu m}{\sqrt{cm}}$ respectively and the result is shown in Figure 7.9.
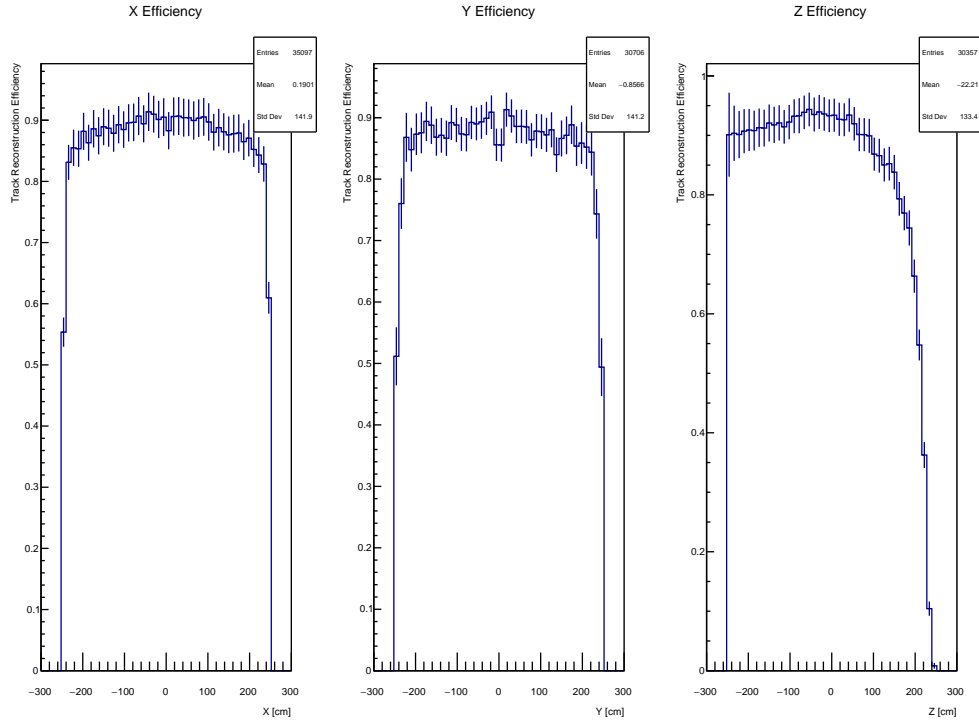

Figure 7.9: Track reconstruction efficiency in the $\hat{x}$, $\hat{y}$, and $\hat{z}$ directions for two times the diffusion constants.

With this increase in diffusion, the software was still able to reconstruct well. Note that because the reconstruction worked well there is a minimal difference in the track starting positions so the plots for 2x diffusion corresponding to Figures 7.4 and 7.5 have been omitted.

7.2.2   4x Diffusion

Now the longitudinal and transverse diffusions are set to 805 and 641.14 $\frac{\mu m}{\sqrt{cm}}$ respectively and the result is shown in Figure 7.10.
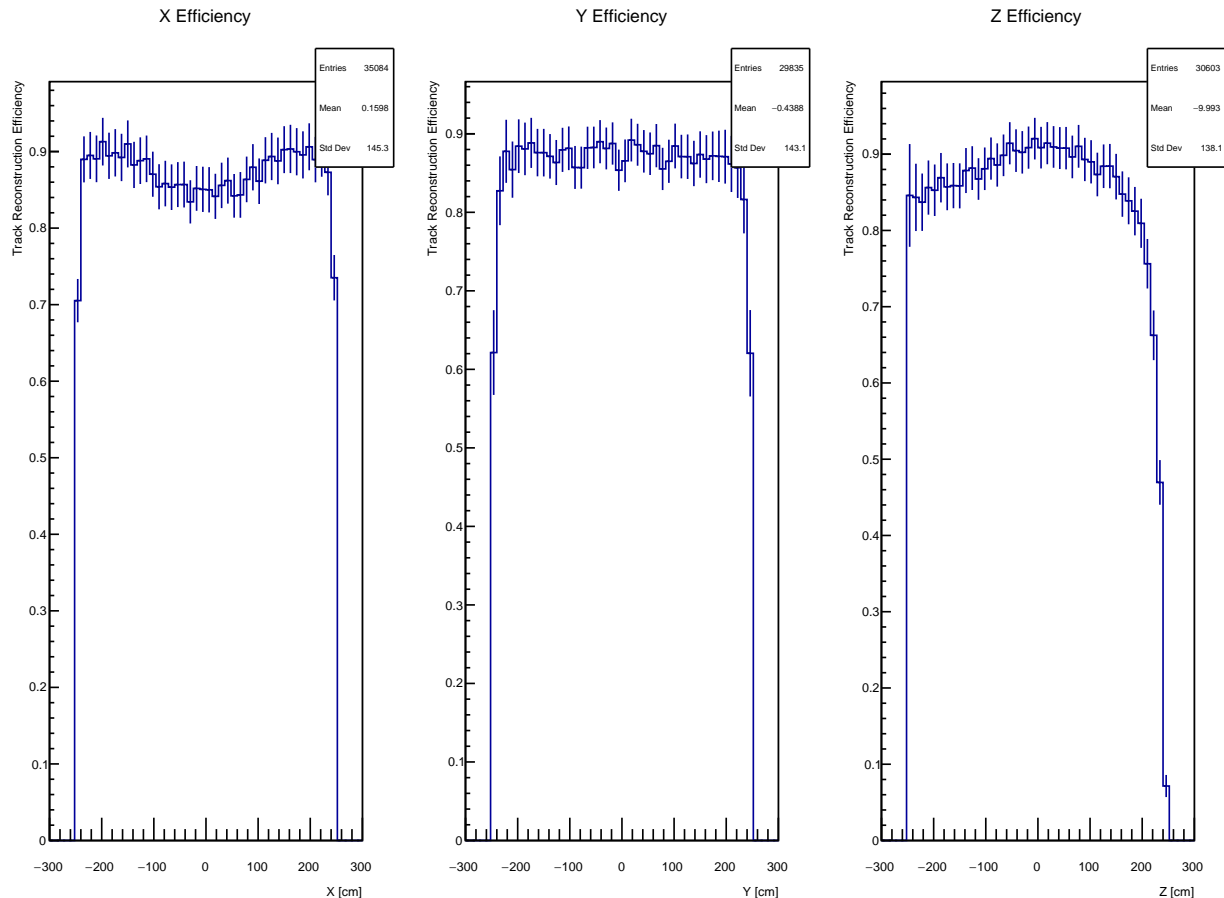

Figure 7.10: Track reconstruction efficiency in the $\hat{x}$, $\hat{y}$, and $\hat{z}$ directions for four times the diffusion constants.

A dip is forming for the efficiency in the $\hat{x}$ direction, however, the loss is only about 5%. This slight drop can still be tolerated. Recall from Chapter 4 that an increase in diffusion of liberated electrons lowers the signal resolution. The more electrons spread out, the more pads in the readout plane gather charge, which in turn, makes the reconstruction

more difficult. Naturally, the longer the drift distance the larger the spread in diffusion, so tracks starting in the center of the detector have a larger drift distance and therefore worse reconstruction efficiency.

7.2.3   10x Diffusion

Now the diffusion is turned up to ten times the nominal case. This means the longitudinal and transverse diffusions are set to 2012.5 and 1602.85 $\frac{\mu\mathrm{m}}{\sqrt{\mathrm{cm}}}$ respectively. The new efficiency plots are shown in Figure 7.11. With the increase in diffusion growing, the simulation software has to run much longer for 100,000 events and as such the ten times diffusion plots were only run with 50,000 events.
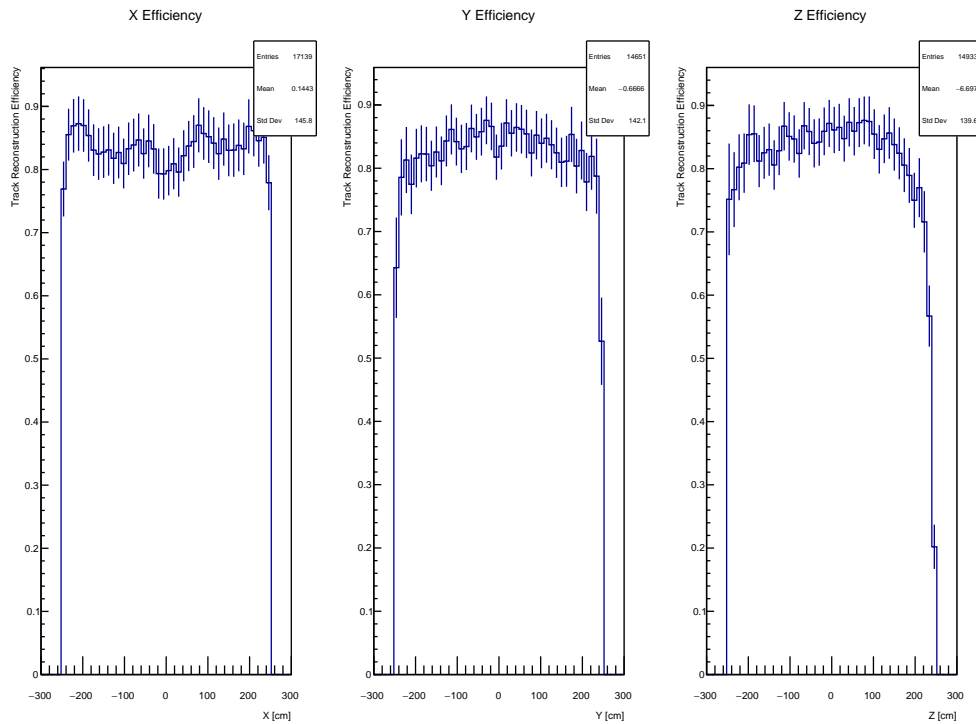

Figure 7.11: Track reconstruction efficiency in the $\hat{x}$, $\hat{y}$, and $\hat{z}$ directions for ten times the diffusion constants.

Now the initial drop from four times is a little more distinct and has a more noticeable

impact in the $\hat{y}$ and $\hat{z}$ directions.

7.2.4   20x Diffusion

Now for the final step, the diffusion jumps to twenty times the nominal case. This corresponds to a longitudinal and transverse diffusions are set to 4025 and 3205.7 $\frac{\mu\text{m}}{\sqrt{\text{cm}}}$ respectively. The result is show in Figure 7.12. Again, for the twenty times diffusion plots, only 50,000 events were simulated.
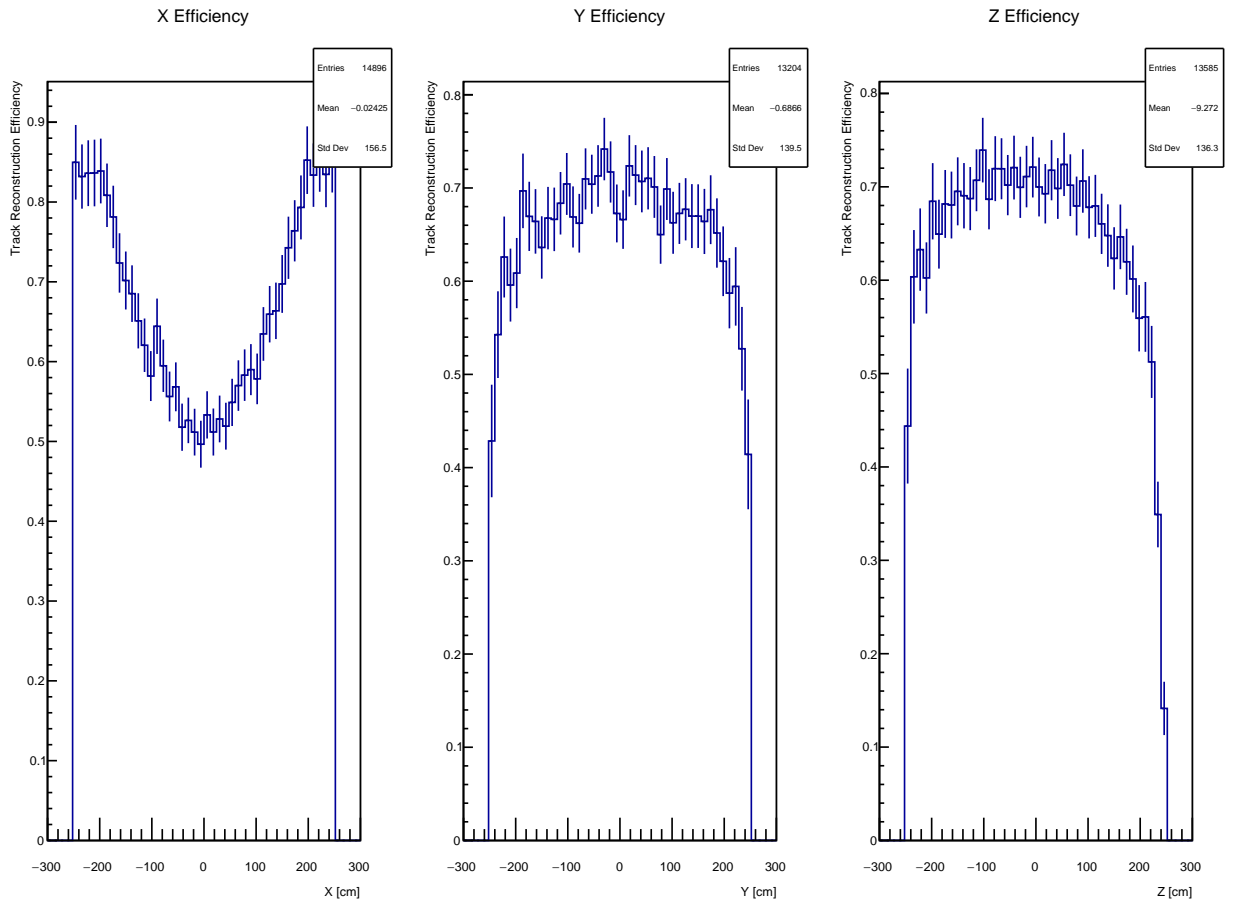

Figure 7.12: Track reconstruction efficiency in the $\hat{x}$, $\hat{y}$, and $\hat{z}$ directions for twenty times the diffusion constants.

This time around the initial drop has become a rather large loss. The reconstruction

efficiency drops by about 35% at worse in the $\hat{x}$ direction and there is significant loss in $\hat{y}$ and $\hat{z}$. To help illustrate this drastic change Figures 7.13 and 7.14 show the disparity between the track reconstructed starting position and the MC simulated track starting positions as in Figures 7.4 and 7.5. Clearly a diffusion of twenty times the nominal setup is not viable for track reconstruction in DUNE's HPgTPC.
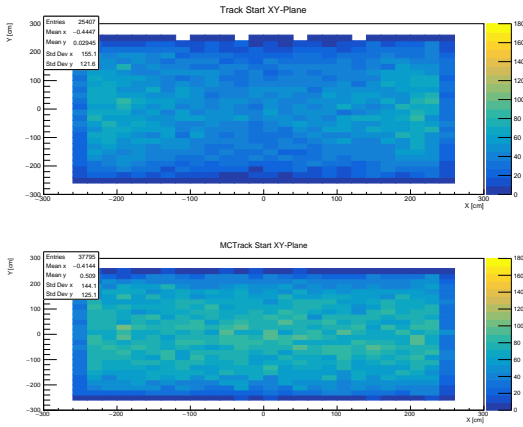

Figure 7.13: Reconstructed track (top) and MC simulated (bottom) track starting positions in the XY-plane for twenty times diffusion.
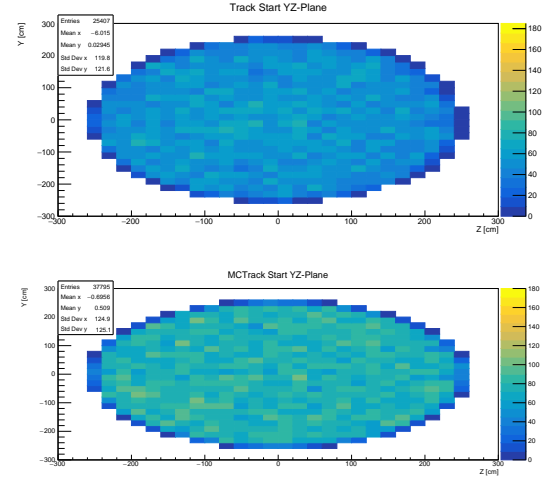

Figure 7.14: Reconstructed track (top) and MC simulated (bottom) track starting positions in the YZ-plane for twenty times diffusion.
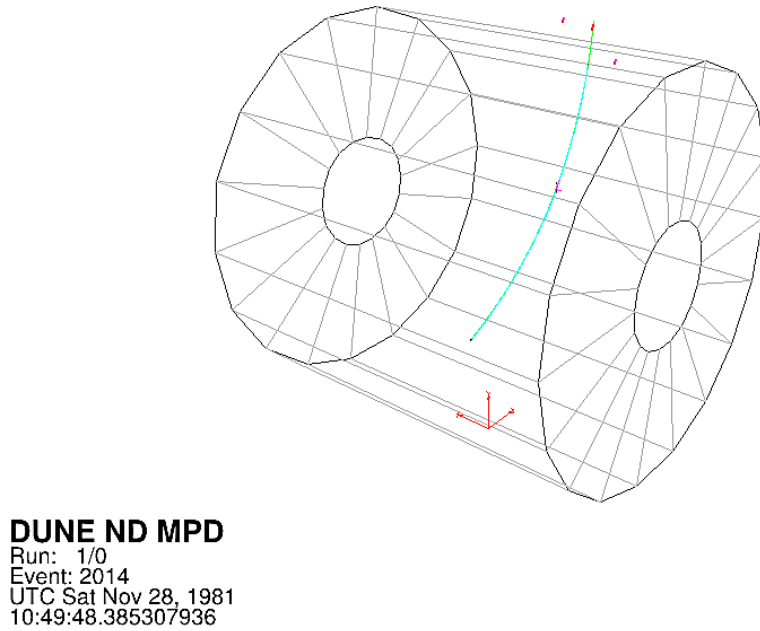
7.3 Protons

Figure 7.15: Event display for an initial high energy (1.236 GeV) proton (cyan). It kicks out a low energy (0.001 GeV) electron (red).

Now the discussion turns to a brief look at reconstructing proton tracks. An example proton reconstruction event display is shown in Figure 7.15. The set up and simulation parameters for the protons was the same as the muons except for the momentum. The new simulation momentum is from $100 \frac{\text{MeV}}{c}$ to $1 \frac{\text{GeV}}{c}$.

Similar to the muon momentum efficiency plot, the protons are easier to reconstructed at higher momentum and at about $300 \frac{\text{MeV}}{c}$ the reconstruction efficiency drops off. This is shown in Figure 7.16. The track reconstruction in each $\hat{x}, \hat{y}$, and $\hat{z}$ takes a similar shape as with the muons, however, the efficiency is slightly lower as shown in Figure 7.17.
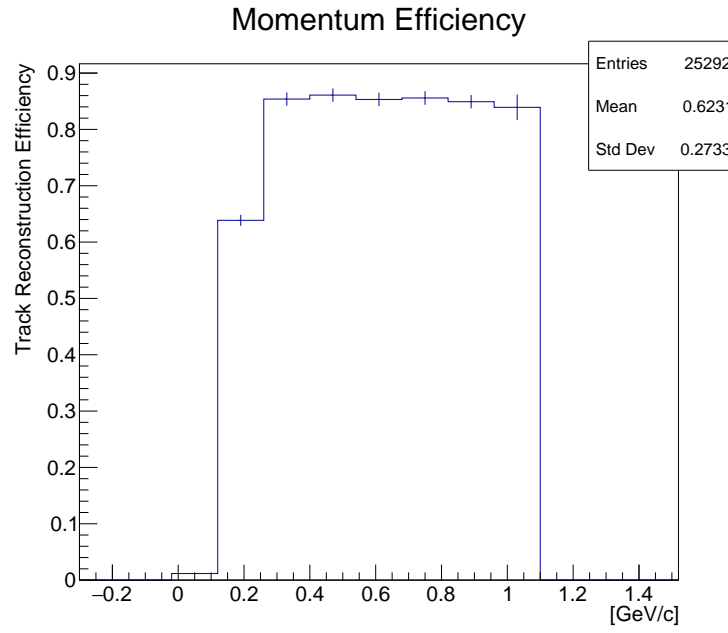
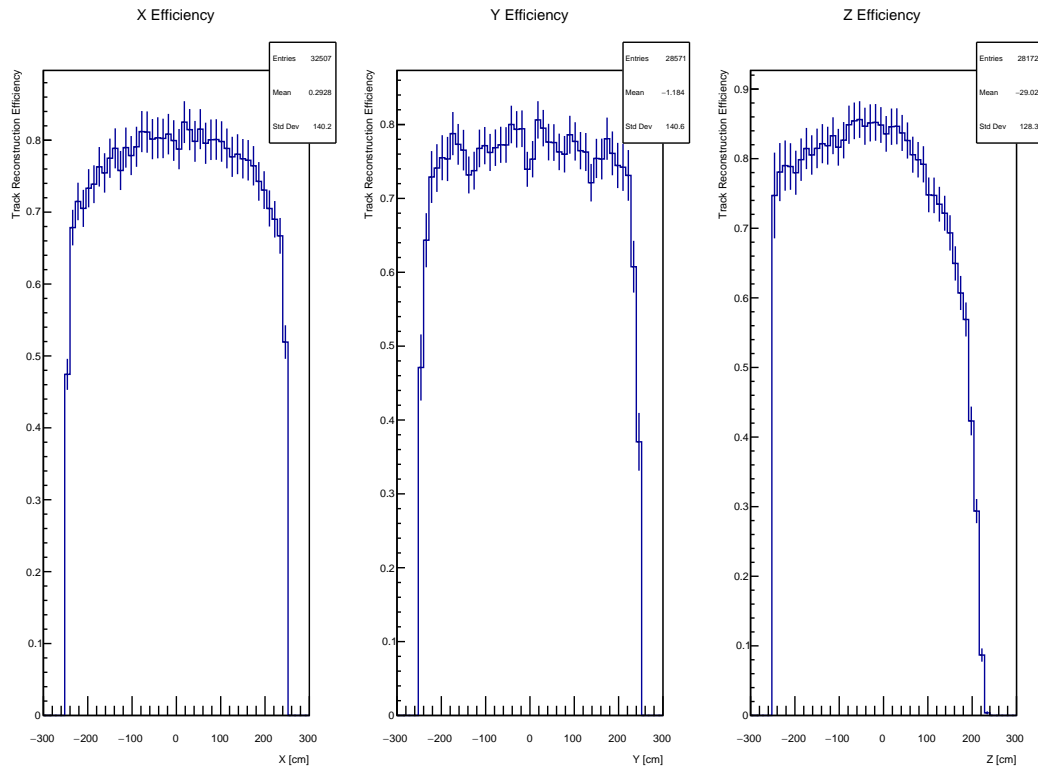Figure 7.16: Track reconstruction efficiency as a function of the proton's momentum.

Figure 7.17: Track reconstruction efficiency in the $\hat{x}$, $\hat{y}$, and $\hat{z}$ directions for protons.

Chapter 8

Conclusions

This chapter concludes the studies and work presented in the thesis. The following sections give a brief summary of the key results and next steps to continue where these studies have left off.

8.1 Summary

There are many factors affecting liberated electrons in DUNE's HPgTPC. The three main factors inspected here were temperature, applied electric field, and the pressure. Given the 2×2 cm^2 resolution of the ECAL surrounding the HPgTPC it is necessary to hold the temperature, electric field, and pressure stable within $\pm2°$ C, $\pm4\,\frac{\text{V}}{\text{cm}}$, and ±0.1 bar each respectively. These conclusions were also summarized in Table 6.2.

Particles that exit the ND-LAr will pass through the ND-GAr where information about their energy, momentum, and sign charge can be determined. Key among these particles are muons. For the nominal case of muons passing through the HPgTPC, reconstruction can be performed with about 80 to 90% efficiency. Tracks can safely be reconstructed with twice or four times as much diffusion, however, performance degrades for diffusion's larger than this. As shown with the twenty times diffusion constants the reconstruction efficiency drops about 50%.

8.2   Looking ahead

One key factor of ND-GAr, that unfortunately, could not be studied here is its magnetic field, as mentioned in Chapter 6. It will be imperative to investigate the electron drift velocity and diffusion once PyBoltz has the ability to look at magnetic fields that are neither parallel nor orthogonal to the electric field. Understanding the regions of the detector where the B-field is not parallel to the E-Field, can give bounds for best region of operation.

The study on track reconstruction presented here was very brief and many things could be expanded on. One of particular interest would be a more complete, in-depth, look at combining multiple PyBoltz drift property outputs as inputs for the GArSoft reconstruction software. This could include determining how efficient the reconstruction is in the regions where the magnetic field is unaligned. In closer connection with the diffusion, to alter the drift velocity with the diffusion in the correct corresponding way (lower drift velocity corresponds to a higher diffusion) would be a valuable study. DUNE will also need to improve the simulation of the electronics and signal readout to better understand the impact of electron loss.

Running PyBoltz

One of the many benefits of writing code in Python is its interpretive ability making it easier to read and a great starting point for many new particle physicists. To run the simulation all one has to do is create a python dictionary which will be the settings under which the simulation will run. When running PyBoltz the user can choose to use the original Boltz.pyx file where they must define all gases and settings independently or using the PyBoltzRun.py wrapper to the Boltz.pyx simulation code. Below is a description of how to use the PyBoltzRun.py wrapper.

Before starting a simulation we must first specify a set of settings for the simulation. Below is an in detail walk through the dictionary that needs to be made; the following is an example from a simulation to understand attachment in Ar:Methane:Oxygen mixture.

```
settings = {"Gases"              : ["ARGON","CH4","OXYGEN"],  #A
            "Fractions"          : [89.98,10,0.02],  #B
            "EField_Vcm"         : 25,   #C
            "Enable_thermal_motion" : 1,   #D
            "Enable_penning"     : 1,    #E
            "Angular_dist_model" : 2,    #F
            "ConsoleOutputFlag"  : 0,    #G
            "Temperature_C"      : 23,   #H
            "Pressure_Torr"      : 3000.25}  # I
```

A: Here set the gas mixture to be simulated. There must be at least one but no more than six.

B: Next tell PyBoltz what the percentage of each gas to use. Order matters so make sure that the percent value index matches with gas index you want.

C: Usually the simulation is run multiple times to plot drift properties as a function of the E-Field (or E/P)[1] so the value chosen when writing the settings dictionary does not matter because it will be changed later in a loop[2].

D: The "Enable_thermal_motion" option turns on and off regular motion of gas particles. This is necessary to get nonzero attachment values and an important part for penning transfer.

E: Penning affects are more clearly seen at high E-fields in the ionisation region however have a small affect on the drift velocity. Setting to 0 turns off and 1 on.

F: Which angular model to use.

G: "ConsoleOutputFlag" just has values printed out during simulation so you can track values being determined.

H: Set the temperature in degrees Celsius of gas mixture. Default is 23.

I: Lastly in this example, set the pressure, in units of Torr, for your gas mixture. The default is 750.062 (1 Bar).

Occasionally these settings are not enough and an error will prompt telling you to increase the energy integration range. This means that PyBoltz was not able to determine the correct integration range to use or it chose an integration range that was too small. To fix this and have the simulation complete set "Max_electron_energy" to the desired value as another

---

[1]   Or any other independent variable you wish to study.

[2]   Here "EField_Vcm"

definition in your dictionary.

Once your gas parameters are set make an instance of the PyBoltzRun.py class[3] then you can run the simulation with

`results = obj.Run(settings).`

All the results are stored in the output of obj.Run('your_settings_dictionary_name') and can be extracted in the following way:

```
results['output_variable'].val
results['output_variable'].err
```

Where '.val' gets the value of the simulation result and '.err' gives you the error on that simulated value. Some of the values are arrays, namely 'Drift_vel' so you have to specify x, y, or z component index (0, 1, 2 respectively). The 'output_variable' can be any of the following:

- 'Drift_vel' the electron drift velocity returned in units of $\frac{mm}{\mu s}$ .val[2] will be the only nonzero entry for majority of simulations unless simulated off axis B-field.

- 'DT' the transverse diffusion coefficient in units of $\frac{cm^2}{s}$.

- 'DT1' the transverse diffusion coefficient in units of $\frac{\mu m}{\sqrt{cm}}$.

- 'DL' the longitudinal diffusion coefficient in units of $\frac{cm^2}{s}$.

- 'DL1' the longitudinal diffusion coefficient in units of $\frac{\mu m}{\sqrt{cm}}$.

- 'MeanEnergy' the average electron energy in units of eV.

- 'Attachment_Rate'[4] η the attachment rate in units of $\frac{attachments}{cm}$.

- 'IonisationRate'[4] α the ionisation rate or first Townsend coefficient reported in units of $\frac{ionpairs}{cm}$.

- 'MCT'[4] the electron mean collision time reported in units of picoseconds.

---

[3] for example obj = PyBoltzRun().

Any .err value is reported as % error of the output variable.

It is nice to study electron drift properties as a function of some independent/controllable variable such as reduced electric field or pressure. With PyBoltzRun.pyx this is very easy to do: create an x-axis array that will be your independent variable and then loop through that array (changing the independent variable in settings dictionary each iteration) storing simulation outputs (y-axis variables) along the way [26]. Here is an in-depth example:

```
settings = {"Gases"                  :  ["ARGON", "OXYGEN"],
            "Fractions"              :  [95.006, 4.994],
            "EField_Vcm"             :  400,
            "Enable_thermal_motion"  :  1,
            "Enable_penning"         :  1,
            "Angular_dist_model"     :  2,
            "ConsoleOutputFlag"      :  0,
            "Temperature_C"          :  23,
            "Pressure_Torr"          :  750.062,
            "Max_electron_energy"    :  10}
obj = PyBoltzRun() #create instance of class
efields = np.arange(0, 100, 10) #independent variable for loop
#create lists to store simulation outputs
DriftVels = []
DT1s=[]
DL1s=[]
DT1s_err=[]
DL1s_err=[]
```

---

4   'Attachment_Rate', 'IonisationRate', and 'MCT' are not set as outputs in the PyBoltzRun.pyx file so you will need to add them. If you are using Boltz.pyx instead then these outputs are stored and you can access them like any other output.

```python
AR = []
AR_err = []
IR = []
IR_err = []
mean_collision_time = []
for e in efields:
    print("════════════════════════════════════")
    print("Running with EField: ", e)
    print("════════════════════════════════════")
    # setting independent variable in settings dictionary
    settings["EField_Vcm"] = e
    # Running simulation storing output to variable named results
    results = obj.Run(settings)
    #appending the dependent variables to their respective lists
    #Z component only nonzero value for this sim
    DriftVels.append(results['Drift_vel'].val[2])
    DT1s.append(results['DT1'].val)
    DT1s_err.append(results['DT1'].err)
    DL1s.append(results['DL1'].val)
    DL1s_err.append(results['DL1'].err)
    AR.append(results['Attachment_Rate'].val)
    AR_err.append(results['Attachment_Rate'].err)
    IR.append(results['IonisationRate'].val)
    IR_err.append(results['IonisationRate'].err)
    mean_collision_time.append(results['MCT'].val)
```

Appendix B

Investigation of PyBoltz Attachment

As mentioned in 6.5 the simulated attachment rates were significantly higher than expected. This section walks through comparisons with simulated attachment and known attachment data namely from [30], [31].

B.1   Pure Oxygen

Since we are concerned about oxygen contamination in DUNE's HPgTPC we reduced the complexity of the mixture and cross checked attachment with pure oxygen as in reference [31], Figures B.1 and B.2 shows the normalized attachment comparison in pure oxygen.
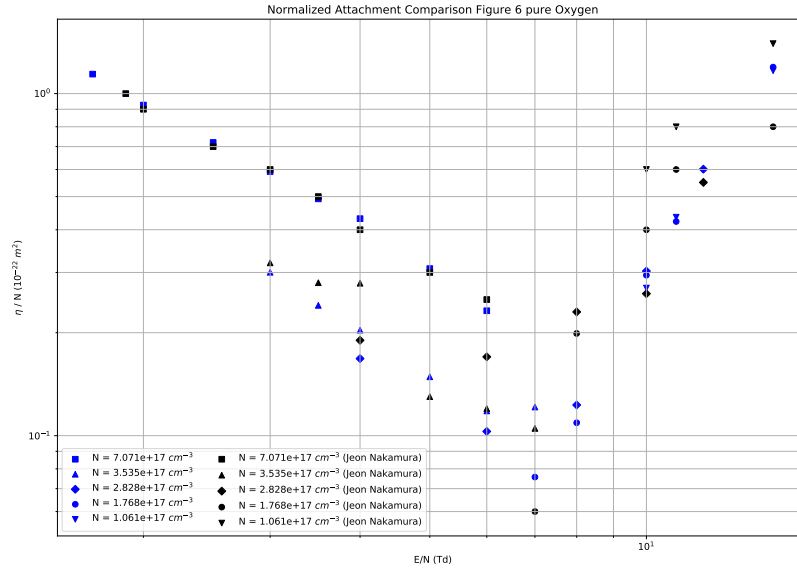

Figure B.1: PyBoltz simulation (blue) compared to Jeon and Nakamura data (black) matches well. MagBoltz agrees with PyBoltz simulation.
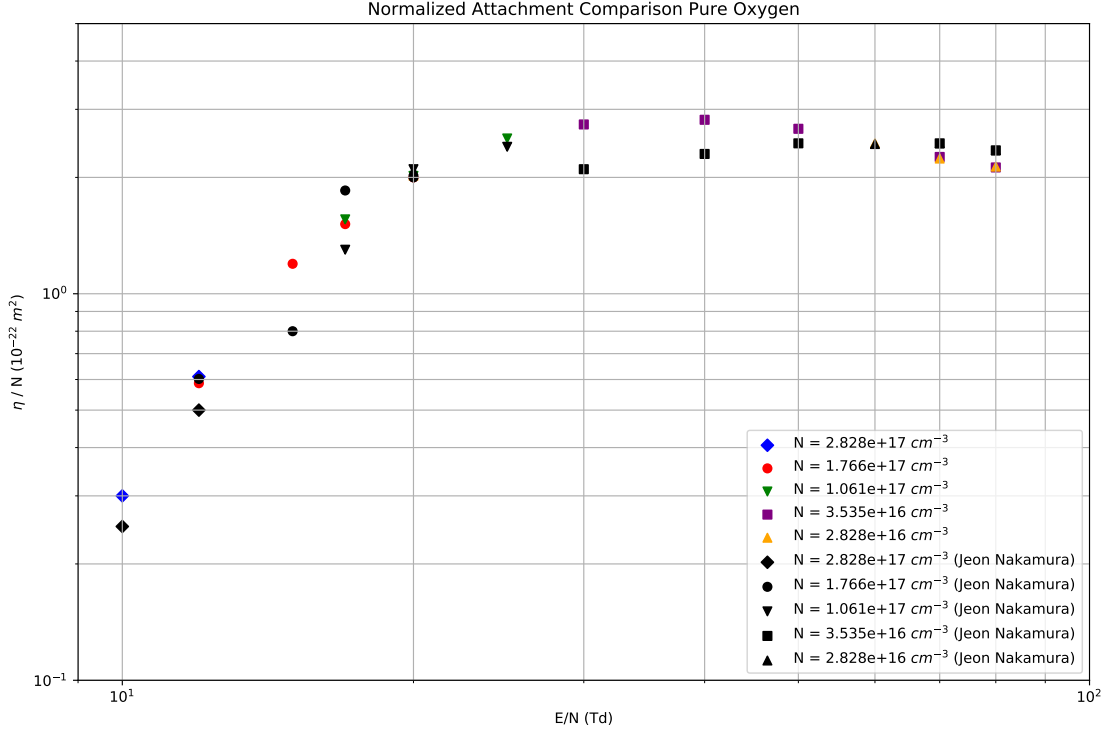
Figure B.2: PyBoltz simulation (colors) compared to Jeon and Nakamura data (black) matches well.

As the figures show the simulation agrees with the experimental data so the issue does not lie with Oxygen alone. However when Argon is introduced there are multiple orders of magnitude of discrepancy between simulation and the corresponding data.

B.2   Argon Oxygen Mixtures

Continuing with our comparison of simulation attachment to reference [31] and increasing the complexity of the mixture to include Argon in two different amounts: 98.99% and 95.006%. In this comparison (shown in Figures B.3 and B.4) we've included the MagBoltz simulation data as well. As these figures depict both simulations agree with each other and are two orders of magnitude larger in 1.01%:98.99% mixture and one order of magnitude larger in 4.994%:95.006% mixture. Although the pressure range is small, reference [31] claims the data was taken in the three body attachment region which can be seen more clearly in

Figure B.4 than in Figure B.3. This error is still quite large and the simulations should be checked further.

Since P-10 is of main interest for the HPgTPC we used reference [30] to cross check PyBoltz attachment in Argon, Methane plus trace amounts of Oxygen. Attachment in reference [30] is reported by the number of surviving electrons as a function of time, where A is the attachment rate in units of μs^{-1} and the number of surviving electrons as a function of distance s, where $\frac{1}{\lambda}$ is the attachment rate reported by PyBoltz:

$$N(t) = N_0 e^{-At}$$
$$N(s) = N_0 e^{\frac{-s}{\lambda}}$$

(B.1)

so to directly compare their attachment rates with simulation attachment we need to convert via

$$\frac{1}{\lambda} = \frac{A}{v}$$

(B.2)

where v is the corresponding electron drift velocity. Figure B.5 shows then the error between the PyBoltz simulation results and [30] experimental data. Once again the error between the data and the simulation is about two orders of magnitude. For another comparison [30], we looked at an even more complex mixture: Argon, Methane, Isobutane and the attachment as a function of parts per million of Oxygen. Table 1a shows the data directly from [30] and table 1b shows the corresponding PyBoltz simulation results. As is shown in the table each simulated attachment is more than 100 times larger than the experimental data. Lastly, Figures B.6, B.7, B.8, and B.9 are presented to show the agreement between MagBoltz and PyBoltz simulations in the E/P region of interest for DUNE's HPgTPC. These plots also reveal that MagBoltz and PyBoltz are simulating attachment as a 3-body process.
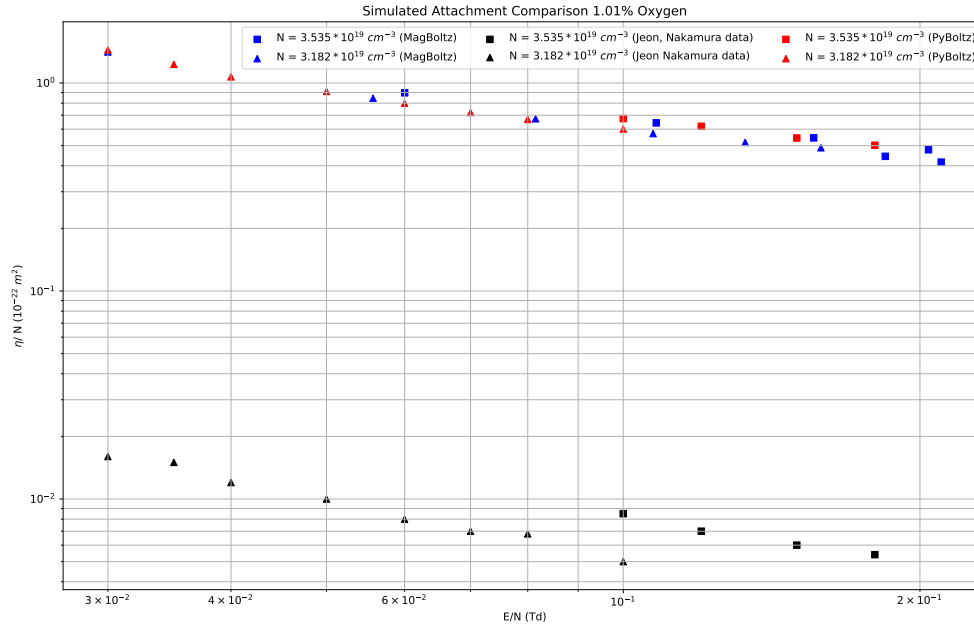
Figure B.3: PyBoltz simulation (red) compared to Jeon and Nakamura data (black) with MagBoltz simulation (blue) in 1.01% oxygen. PyBoltz and MagBoltz simulations agree with each other but are 2 orders of magnitude off.
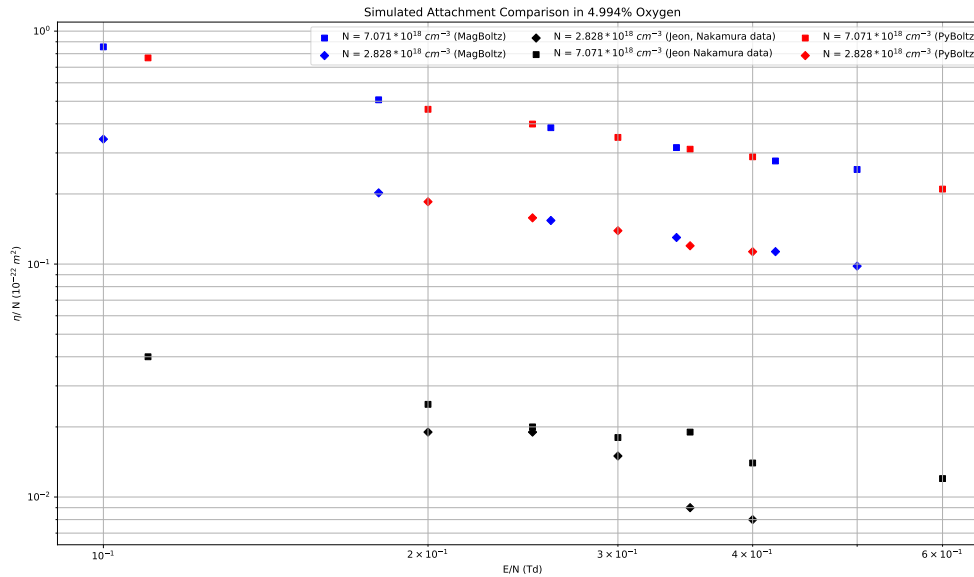

Figure B.4: PyBoltz simulation (red) compared to Jeon and Nakamura data (black) with MagBoltz simulation (blue) in 4.994% oxygen. PyBoltz and MagBoltz simulations agree with each other but are an order of magnitude off.
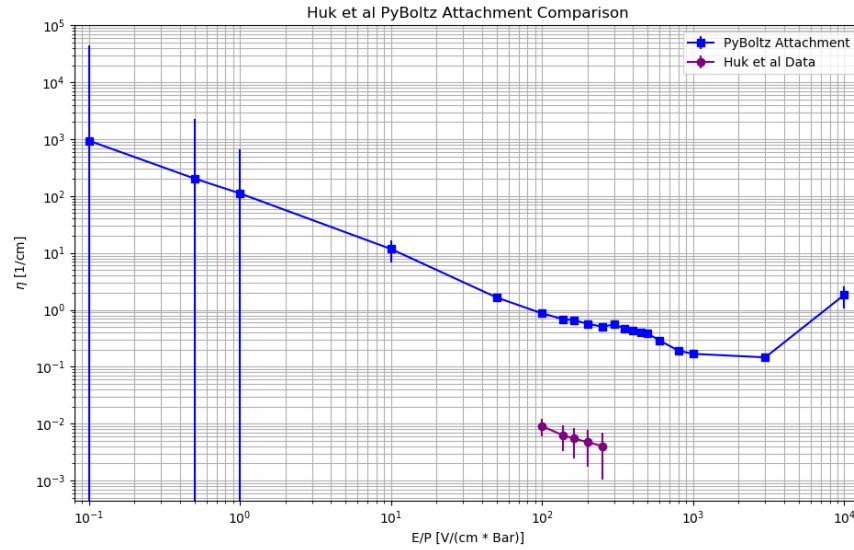
Figure B.5: Huk et al PyBoltz attachment comparison of p-10 + 200 ppm of O_2. PyBoltz is about two orders of magnitude larger
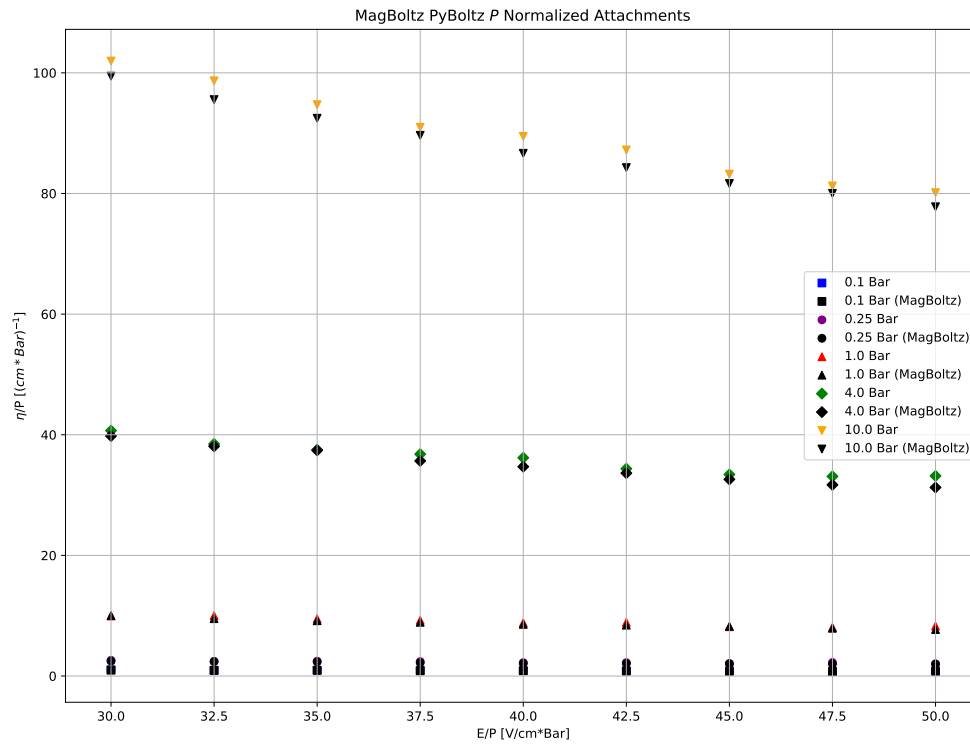

Figure B.6: MagBoltz and PyBoltz pressure normalized attachment comparison in 1.01% Oxygen 99% Argon.

Table B.1: PyBoltz Output for comparison of Huk et al table 2. 88:10:2 argon:methane:isobutane + oxygen mixture at 4 Bar (assumed temperature of 23 ^{o}C)

| E/P $[\frac{V}{cm*Bar}]$	$O_2[ppm]$	v $[\frac{cm}{\mu s}]$	Attachment rate $[\mu s^{-1}]$
Huk *et al* table 2			
	50	4.67	0.062 ± 0.005
	100	4.67	0.111 ± 0.005
100	200	4.67	0.215 ± 0.007
	300	4.67	0.353 ± 0.011
	440	4.67	0.566 ± 0.019
	50	5.43	0.037 ± 0.005
	100	5.43	0.066 ± 0.005
200	200	5.43	0.130 ± 0.006
	300	5.43	0.199 ± 0.008
	440	5.43	0.287 ± 0.009
PyBoltz simulation results			
	50	4.53	$(1.459) \pm (3.29 * 10^{-4})$
	100	4.53	$(2.858) \pm (9.01 * 10^{-4})$
100	200	4.52	$(6.143) \pm (2.87 * 10^{-3})$
	300	4.52	$(8.606) \pm (4.75 * 10^{-3})$
	440	4.51	$(13.12) \pm (8.93 * 10^{-3})$
	50	5.42	$(0.997) \pm (1.62 * 10^{-4})$
	100	5.43	$(2.058) \pm (4.77 * 10^{-4})$
200	200	5.42	$(3.978) \pm (1.29 * 10^{-3})$
	300	5.42	$(6.157) \pm (2.48 * 10^{-3})$
	440	5.42	$(8.726) \pm (4.18 * 10^{-3})$
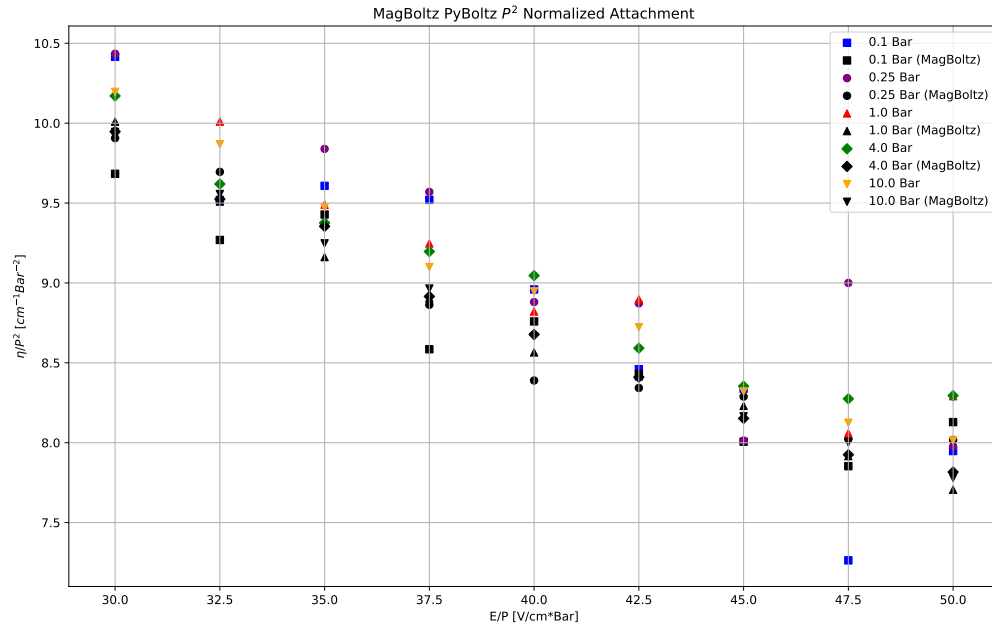
Figure B.7: MagBoltz and PyBoltz pressure squared normalized attachment comparison in 1.01% Oxygen 99% Argon.
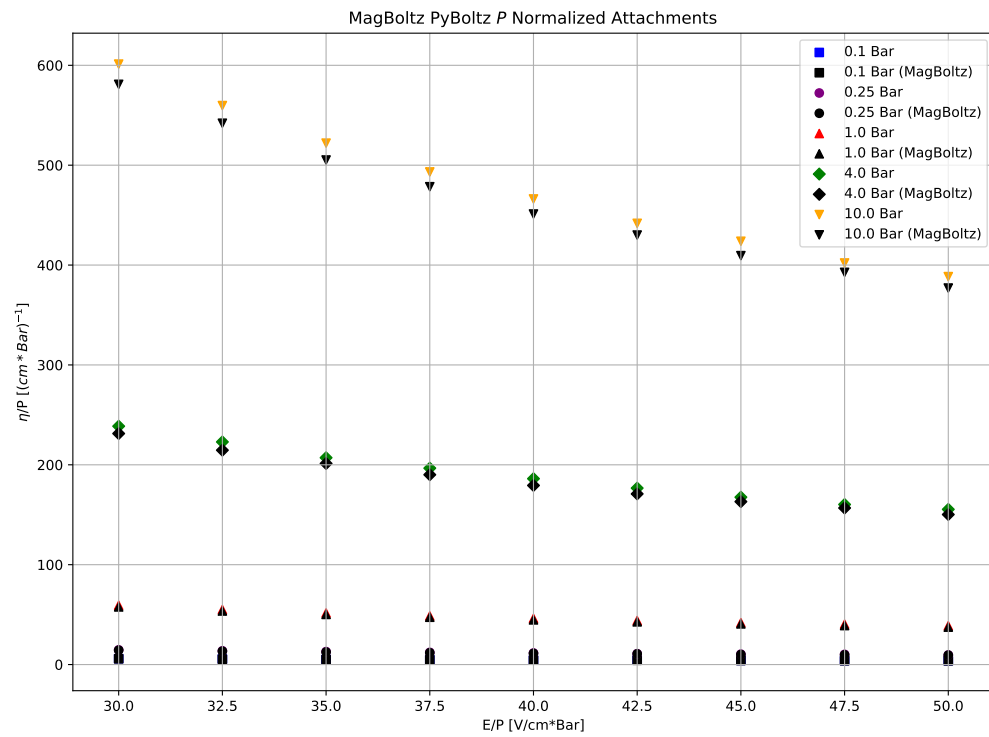

Figure B.8: MagBoltz and PyBoltz pressure normalized attachment comparison in 4.994% Oxygen 95.006% Argon.
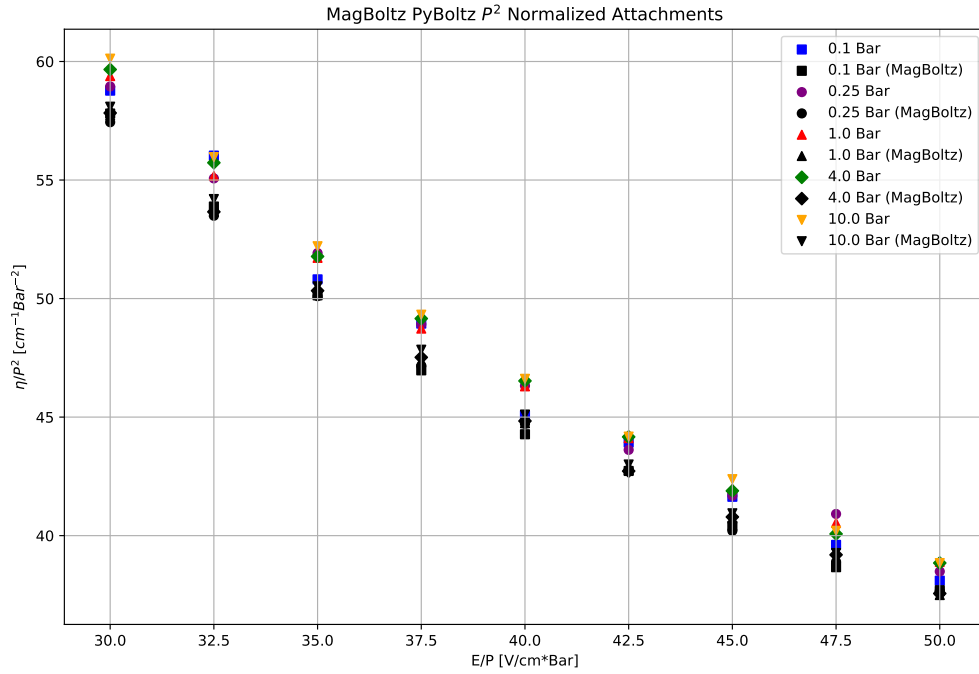
Figure B.9: MagBoltz and PyBoltz pressure squared normalized attachment comparison in 4.994% Oxygen 95.006% Argon.
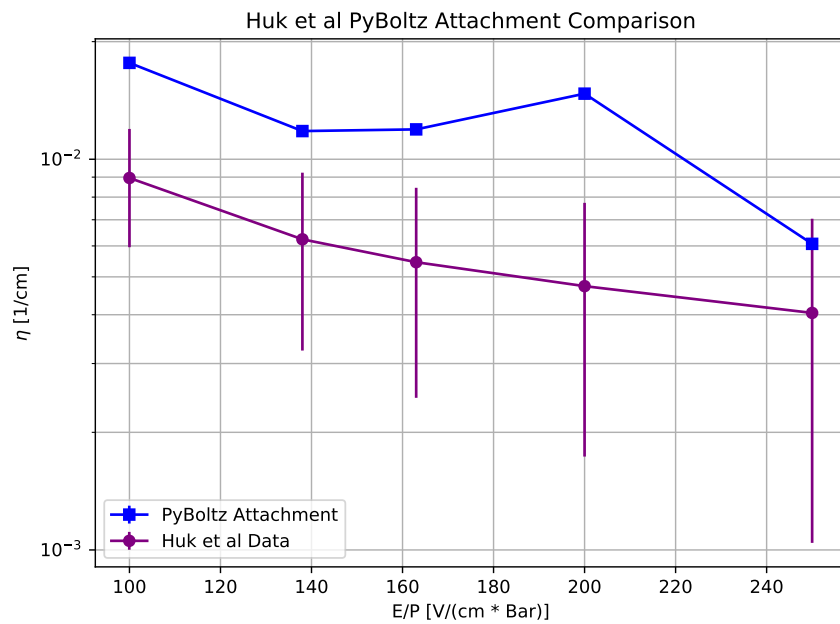

Figure B.10: Adjusted 3-body attachment scaling factor for Argon Methane Oxygen mixture compared with Huk et al experimental attachment.

Bibliography

[1] D. Griffiths, *Introduction to Elementary Particles*, 2nd. Wiley-VCH, 2008, ISBN: 9783527406012.

[2] D. McIntyre, *Quantum Mechanics: A Paradigms Approach*. Boston, Massachusetts: Pearson, 2012.

[3] B. Abi *et al.*, "Deep Underground Neutrino Experiment (DUNE), Far Detector Technical Design Report, Volume II: DUNE Physics," Feb. 2020. arXiv: `2002.03005 [hep-ex]`.

[4] R. Acciarri *et al.*, "Long-Baseline Neutrino Facility (LBNF) and Deep Underground Neutrino Experiment (DUNE) Conceptual Design Report Volume 1: The LBNF and DUNE Projects," 2016. DOI: `arXiv:1601.05471`. arXiv: `1601.05471 [physics.ins-det]`. [Online]. Available: `https://arxiv.org/abs/1601.05471`.

[5] S. Born, "Identifying V0 Decays in the DUNE High-Pressure Gaseous Argon TPC," Undergraduate Honors Thesis, University of Colorado Boulder, 2020. [Online]. Available: `https://scholar.colorado.edu/concern/undergraduate_honors_theses/x059c836m`.

[6] C. Giunti and C. W. Kim, *Fundamentals of Neutrino Physics and Astrophysics*. UOP Oxford, 2007, ISBN: 9780198508717.

[7] K. Dochen, "Diamond Muon Monitors for the Deep Underground Neutrino Experiment," Undergraduate Honors Thesis, University of Colorado Boulder, 2017. [Online]. Available: `https://scholar.colorado.edu/concern/undergraduate_honors_theses/dz010q498`.

[8] B. R. Martin and G. Shaw, *Nuclear and Particle Physics*, 3rd. Wiley, 2019.

[9] T. D. Lee and C. N. Yang, "Question of Parity Conservation in Weak Interactions," *Phys. Rev.*, vol. 104, pp. 254–258, 1 1956. DOI: `10.1103/PhysRev.104.254`. [Online]. Available: `https://link.aps.org/doi/10.1103/PhysRev.104.254`.

[10] C. S. Wu, E. Ambler, R. W. Hayward, D. D. Hoppes, and R. P. Hudson, "Experimental Test of Parity Conservation in Beta Decay," *Phys. Rev.*, vol. 105, pp. 1413–1415, 4 1957. DOI: `10.1103/PhysRev.105.1413`. [Online]. Available: `https://link.aps.org/doi/10.1103/PhysRev.105.1413`.

[11] M. Thomson, *Modern Particle Physics*. University of Cambridge, 2013.

[12] "Neutrino Oscillations." [Online]. Available: `https://ifirse.icise.vn/nugroup/Neutrino-Oscillations.html`.

[13] H. Nunokawa, S. Parke, and J. W. Valle, "CP Violation and Neutrino Oscillations," *Progress in Particle and Nuclear Physics*, vol. 60, pp. 338–402, 2008, ISSN: 0146-6410. DOI: `10.1016/j.ppnp.2007.10.001`. [Online]. Available: `http://dx.doi.org/10.1016/j.ppnp.2007.10.001`.

[14] M. Bass *et al.*, "Baseline Optimization for the Measurement of CP Violation, Mass Hierarchy, and $\theta 23$ Octant in a Long-Baseline Neutrino Oscillation Experiment," *Physical Review D*, vol. 91, Mar. 2015, ISSN: 1550-2368. DOI: `10.1103/physrevd.91.052015`. [Online]. Available: `http://dx.doi.org/10.1103/PhysRevD.91.052015`.

[15] S. Gitalov, "Monte Carlo Simulation of the DUNE Stopped Muon Monitor Prototype Exposed to Cosmic Ray Muons," Undergraduate Honors Thesis, University of Colorado Boulder, 2020. [Online]. Available: `https://scholar.colorado.edu/concern/undergraduate_honors_theses/08612p43k`.

[16] P. Zyla *et al.*, "Review of Particle Physics," *PTEP*, vol. 2020, p. 083C01, 2020. DOI: `10.1093/ptep/ptaa104`.

[17] B. Kayser, "Neutrino Physics," SLAC Summer Institute on Particle Physics, 2004. [Online]. Available: `https://www.slac.stanford.edu/econf/C040802/papers/L004.PDF`.

[18] X. Qian and P. Vogel, "Neutrino Mass Hierarchy," *Progress in Particle and Nuclear Physics*, vol. 83, pp. 1–30, 2015, ISSN: 0146-6410. DOI: `10.1016/j.ppnp.2015.05.002`. [Online]. Available: `http://dx.doi.org/10.1016/j.ppnp.2015.05.002`.

[19] Fermilab, "Deep Underground Neutrino Experiment," 2020. [Online]. Available: `https://www.dunescience.org`.

[20] K. Duffy, "High-Pressure Gaseous Argon TPC for the DUNE Near Detector," 2019. arXiv: `1910.06422 [physics.ins-det]`.

[21] W. Leo, *Techniques for Nuclear and Particle Physics Experiments*. Springer, 1994.

[22] F. Sauli, *Gaseous Radiation Detectors: Fundamentals and Applications*. Cambridge University Press, 2014. [Online]. Available: `https://ebookcentral.proquest.com`.

[23] Ö. Şahin, İ. Tapan, E. N. Özmutlu, and R. Veenhof, "Penning Transfer in Argon-Based Gas Mixtures," *Journal of Instrumentation*, vol. 5, P05002–P05002, 2010. DOI: `10.1088/1748-0221/5/05/p05002`. [Online]. Available: `https://doi.org/10.1088/1748-0221/5/05/p05002`.

[24] J. Alme, Y. Andres, H. Appelshauser, *et al.*, "The ALICE TPC, a Large 3-Dimensional Tracking Device with Fast Readout for Ultra-High Multiplicity Events," *Nuclear Instruments and Methods A*, vol. 622, pp. 316–367, 2010, ISSN: 0168-9002.

[25] G. F. Knoll, *Radiation Detectors and Measurement*, 4th. Wiley, 2010.

[26] B. Al Atoum, S. Biagi, D. González-Díaz, B. Jones, and A. McDonald, "Electron Transport in Gaseous Detectors with a Python-Based Monte Carlo Simulation Code," *Computer Physics Communications*, 2020.

[27] S. Biagi, "Monte Carlo Simulation of Electron Drift and Diffusion in Counting Gases Under the Influence of Electric and Magnetic Fields," *Nucl. Instrum. Meth. A*, vol. 421, pp. 234–240, 1999. DOI: `10.1016/S0168-9002(98)01233-9`.

[28] B. Rebel *et al.*, "Garsoft," 2021. [Online]. Available: `https://cdcvs.fnal.gov/redmine/projects/garsoft`.

[29] S. Biagi, "Private communication."

[30] M. Huk, P. Igo-Kemenes, and A. Wagner, "Electron Attachment to Oxygen, Water, and Methanol, in Various Drift Chamber Gas Mixtures," *Nuclear Instruments and Methods in Physics Research Section A: Accelerators, Spectrometers, Detectors and Associated Equipment*, vol. 267, pp. 107–119, 1988, ISSN: 0168-9002. [Online]. Available: `http://www.sciencedirect.com/science/article/pii/0168900288906353`.

[31] B. H. Jeon and Y. Nakamura, "Measurement of Electron Attachment Coefficient in Oxygen and Oxygen-Argon Mixtures," *IEEJ Transactions on Fundamentals and Materials*, pp. 874–879, 1998.